

---

# THE SHAPE OF ATTRACTION IN UMAP: EXPLORING THE EMBEDDING FORCES IN DIMENSIONALITY REDUCTION

---

**Mohammad Tariqul Islam<sup>1,2</sup>, Jason W. Fleischer<sup>1\*</sup>**

<sup>1</sup>Department of Electrical and Computer Engineering, Princeton University, Princeton, NJ 08544, USA

<sup>2</sup>Media Lab, Massachusetts Institute of Technology, Cambridge, MA 02139, USA  
{mtislam, jasonf}@princeton.edu

## ABSTRACT

Uniform manifold approximation and projection (UMAP) is among the most popular neighbor embedding methods. The method relies on attractive and repulsive forces among high-dimensional data points to obtain a low-dimensional embedding. In this paper, we analyze the forces to reveal their effects on cluster formations and visualization. Repulsion emphasizes differences, controlling cluster boundaries and inter-cluster distance. Attraction is more subtle, as attractive tension between points can manifest simultaneously as attraction and repulsion in the lower-dimensional mapping. This explains the need for learning rate annealing and motivates the different treatments between attractive and repulsive terms. Moreover, by modifying attraction, we improve the consistency of cluster formation under random initialization. Overall, our analysis makes UMAP and similar embedding methods more interpretable, more robust, and more accurate.

## 1 Introduction

The current era is characterized by a deluge of high-dimensional data. Dimensionality reduction (DR) techniques have emerged as tools for exploratory analysis of such data by visualizing the underlying structure. The most popular methods,  $t$ -distributed stochastic neighbor embedding [1] and uniform manifold approximation and projection (UMAP) [2] are grounded in the attraction-repulsion dynamics that bring similar data points closer while pushing dissimilar ones apart. As unsupervised algorithms, these do not rely on labeled data; instead, they identify and preserve the intrinsic structure of high-dimensional data by leveraging local (attractive) and global (repulsive) relationships (forces). This makes these algorithms particularly well-suited for tasks such as clustering [3], exploratory data analysis [4], anomaly detection in semiconductor manufacturing [5], visual search [6], time series analysis [7], studying representation convergence [8], and outlier image detection [9], where visualizing hidden patterns in unlabeled data is critical and meaningful. By learning the embeddings in a data-driven, label-free manner, DR exemplifies the power of unsupervised methods to distill complex data into easily interpretable forms.

Building upon the attraction-repulsion principle, newer methods have emerged [10, 11, 12, 13, 14, 15], each designed to emphasize specific aspects of the data. Despite their relevance in diverse applications, these methods often rely on heuristic practices that may fail to give meaningful interpretations. Moreover, DR introduces distortions that are unavoidable [16]. Thus, it is imperative to have a deeper understanding of the algorithms so that practitioners can provide better interpretations of the embeddings, avoid spurious structures, and optimize performance.

In practice, these algorithms achieve compact clusters using a variety of techniques, including specific initialization, learning rate schedule, and kernel function tuning. However, the underlying dynamics of the attractive and repulsive forces, responsible for cluster formation, have not been thoroughly investigated. Furthermore, the essential tunable parameters are concealed within abstract functional forms, making it harder to explain the algorithms.

In this paper, we decompose the forces into their constituent parts and extract the functional shapes of attraction and repulsion. We find that the necessity of learning rate annealing, the challenge of providing consistent output under random initialization, and the origin of cluster formation rely on attraction. Repulsive forces primarily govern

---

\*Corresponding Author

inter-cluster distances. By exploring the parameter space, we expand the possibilities of cluster formation beyond the conventional boundaries of neighbor embedding methods.

Our specific contributions are:

1. We formulate attraction and repulsion shapes from the attractive and repulsive forces, establish the conditions for contraction and expansion of distance, and provide a fresh perspective for these algorithms (Section 4).
2. We show that the attraction shape of UMAP causes the counterintuitive concept of both contraction and expansion of distance. We also discuss how attraction influences the learning rate annealing scheme (Section 5).
3. We modify the attraction shape to improve the consistency of embedding under random initialization. This indicates the encoding of a unique structure (Section 5.1).
4. Analyzing repulsion shapes, we provide a deeper understanding of cluster formation and regulating inter-cluster distance (Section 5.2).
5. We compare attraction and repulsion shapes of UMAP and NEG- $t$ -SNE, unveil the fundamental distinctions between them, and characterize the stability of the algorithms (Section 6).

In the main text, we focus on UMAP and extend our analysis to additional algorithms in the Appendices. The codes used in the research are available at [https://github.com/tariqul-islam/explaining\\_neighbor\\_embedding](https://github.com/tariqul-islam/explaining_neighbor_embedding).

## 2 Related Works

The origin of modern iterative graph-based neighbor embedding algorithms can be traced to stochastic neighbor embedding (SNE) [17] and its extension using the  $t$ -distribution ( $t$ -SNE) [1]. Both methods use a dense graph in which each point in a dataset has a pairwise relation with all the others, regardless of whether they are similar to each other or not. Moreover, the weights of the graphs are normalized to give a notion of probability distribution. Other concurrent methods, including locally linear embedding [18] and Laplacian Eigenmaps (LE) [19], used a  $k$ -nearest neighbor ( $k$ -NN) graph of pairwise interaction. Known as spectral methods, these algorithms rely on Eigenvalue decomposition. Subsequent work by Tang et al. [20] incorporated the  $k$ -NN graph in the iterative approach and removed normalization in the lower dimension. This approach was further extended by McInnes et al. [2] in UMAP, where the normalization step was removed altogether (both in high and low dimension) and the embedding was obtained using pairwise interactions alone. The optimization steps use an explicit attractive force to preserve the local neighborhood and a repulsive force to keep dissimilar points apart.

There has been considerable progress in understanding and explaining the relationship among these algorithms. An early analysis of SNE found that if the data is well-clustered in the original space, then they are well-clustered in the embedding space [21]. A similar analysis for  $t$ -SNE by Linderman and Steinerberger [22] showed that the number of clusters in the embedding space is a lower bound on the number of clusters in the original space. This was followed up in further characterization [23, 24, 25]. Since  $t$ -SNE and UMAP originate from the same underlying framework (but with drastically different visualizations), a major undertaking in the literature has been to find the connection between them [26, 27, 28, 29]. Böhm et al. [26] theorized that methods like Laplacian Eigenmap, ForceAtlas2 [30], UMAP, and  $t$ -SNE are all samples from the same underlying spectrum. Indeed, LE and  $t$ -SNE's are connected by the early exaggeration phase [24]. The connection between UMAP and  $t$ -SNE can be related through contrastive estimation [27]. Around the same time, [31] independently discovered the relation of contrastive learning and SNE. Recent approaches offer a probabilistic perspective [29, 32], employ kernel techniques [33], and utilize information geometry [34] to explain dimensionality reduction.

## 3 Uniform Manifold Approximation and Projection

UMAP constructs a high-dimensional graph of the dataset  $X = \{x_i \in R^n | i = 1, \dots, N\}$  by the following system of equations:

$$p_{i|j} = \begin{cases} \exp\left(-\frac{d(\mathbf{x}_i, \mathbf{x}_j) - \rho_i}{\sigma_i}\right) & \text{if } x_j \in \text{KNN}(\mathbf{x}_i, k) \\ 0 & \text{otherwise} \end{cases}, \quad (1)$$

$$\rho_i = \min_{\mathbf{x}_j \in \text{KNN}(\mathbf{x}_i, k)} d(\mathbf{x}_i, \mathbf{x}_j), \quad (2)$$

where  $\text{KNN}(\mathbf{x}_i, k)$  is the set of  $k$ -nearest neighbors of the point  $\mathbf{x}_i$  and  $\sigma_i$  is a scaling parameter such that  $\sum_j p_{i|j} = \log_2(k)$ . The graph is then symmetrized by a t-conorm:

$$p_{i,j} = p_{i|j} + p_{j|i} - p_{i|j}p_{j|i}. \quad (3)$$

The graph of the low-dimensional data  $Y = \{y_i \in \mathbb{R}^d | i = 1, \dots, N\}$  is given by a differentiable function

$$q_{ij} = \frac{1}{1 + a(\|\mathbf{y}_i - \mathbf{y}_j\|_2^2)^b}, \quad (4)$$

where the parameters  $a$  and  $b$  determine the density of the mapping and are chosen by fitting  $q_{ij}$  to

$$\Psi(d_{ij}) = \begin{cases} 1 & \text{if } \|\mathbf{y}_i - \mathbf{y}_j\|_2 < m_d \\ \exp(-(d_{ij} - m_d)) & \text{otherwise} \end{cases} \quad (5)$$

where  $m_d$  regulates the distance between the two nearest low-dimensional points.

UMAP aims to minimize the following cross-entropy loss function:

$$\mathcal{L} = \sum_{i,j} (-p_{ij} \log(q_{ij}) - (1 - p_{ij}) \log(1 - q_{ij})). \quad (6)$$

The first term provides an attractive force and the second term provides a repulsive force. Instead of optimizing every point in each iteration, UMAP takes the negative sampling approach [35, 20]. For each edge with  $p_{ij} > 0$ , named a positive edge, several edges are sampled randomly, named negative edges. The attractive force is applied on the positive edge:

$$y_i^{t+1} = y_i^t + \lambda \nabla_{y_i^t} \log(q_{ij}), \quad (7)$$

$$y_j^{t+1} = y_j^t + \lambda \nabla_{y_j^t} \log(q_{ij}), \quad (8)$$

and the repulsive force is applied on the negative edges:

$$y_i^{t+1} = y_i^t + \lambda \nabla_{y_i^t} \log(1 - q_{ij}), \quad (9)$$

where  $\lambda(> 0)$  is the learning rate and  $t$  is the step number. Note that  $y_j$  is not updated for negative edges.

## 4 Attraction and Repulsion Shapes

The action of the updates (7-9) can be simplified by decomposing the gradients  $\nabla_{y_i^t} \log(q_{ij})$  ( $\nabla_{y_i^t} \log(1 - q_{ij})$ ) into a scalar coefficient dependent on the distance  $\|y_i - y_j\|_2$  acting on the vector  $(y_i - y_j)$ . We call this scalar coefficient the attraction (repulsion) shape. While we use UMAP as a specific example, this formalism applies to any method that relies on attraction and repulsion.

By writing  $\nabla_{y_i^t} \log(q_{ij}) = f_a(\zeta^t)(y_i^t - y_j^t)$ , where  $\zeta = \|y_i - y_j\|_2$ , we can update the equations of a positive edge as

$$y_i^{t+1} = y_i^t + \lambda f_a(\zeta^t)(y_i^t - y_j^t), \quad (10)$$

$$y_j^{t+1} = y_j^t - \lambda f_a(\zeta^t)(y_i^t - y_j^t). \quad (11)$$

Here,  $f_a : \mathbb{R}_{\geq 0} \rightarrow \mathbb{R}_{\leq 0}$  is the attraction shape, and we use the fact that for Euclidean metric,  $\nabla_{y_i^t} \log(q_{ij}) = -\nabla_{y_j^t} \log(q_{ij})$ . Similarly, we reformulate the update equation of a negative edge as

$$y_i^{t+1} = y_i^t + \lambda f_r(\zeta^t)(y_i^t - y_j^t), \quad (12)$$

$$y_j^{t+1} = y_j^t, \quad (13)$$

where  $f_r : \mathbb{R}_{\geq 0} \rightarrow \mathbb{R}_{\geq 0}$  is the repulsion shape.

Such decomposition has appeared previously, e.g., in [2, 11, 33], but their formulations and utilization vary. The original UMAP paper [2] used it as a computational trick for fast processing, while Draganov et al. [33] used it for comparing different algorithms from the kernel perspective. In both cases, the primary focus was computing the derivative. Here, we treat the decompositions as independent functions that can take various forms. A similar approach was used earlier by Agrawal et al. [11], but they expressed the decomposition in terms of a scalar coefficient and a unit vector  $((y_i - y_j)/\|y_i - y_j\|_2)$  to emphasize the magnitude of the forces. The discussion below shows that our shape decomposition is more illuminating than the magnitude alone.

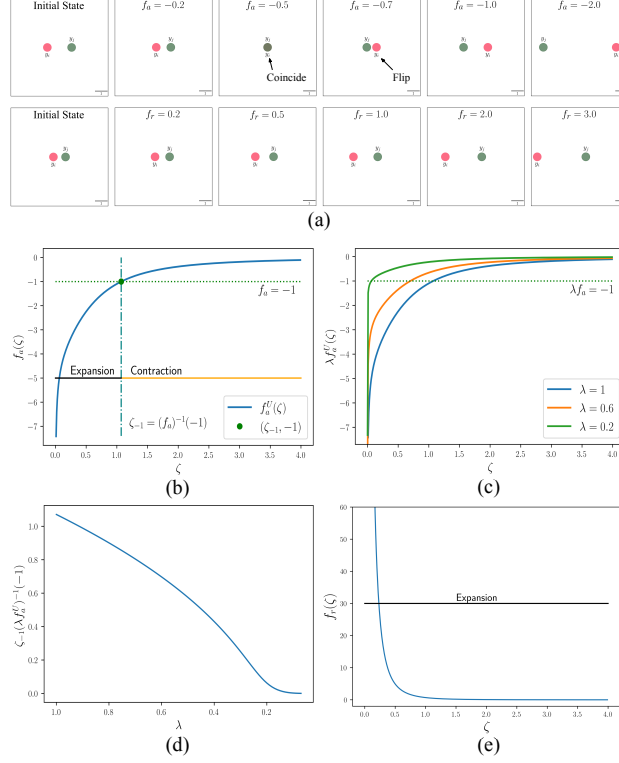


Figure 1: Attraction and repulsion shapes in UMAP. (a) Effect of different values of  $f_a$  (top) and  $f_r$  (bottom) on a pair. (b) Attraction shape of UMAP. (c) Effective attraction shape ( $\lambda f_a$ ) for various learning rates  $\lambda$ . (d) Minimum distance of contraction ( $\zeta_{-1}$ ) as  $\lambda$  decreases. (e) Repulsion shape of UMAP. Parameters:  $a = 1.576$  and  $b = 0.89$ .

#### 4.1 Theoretical Considerations

In this section, we establish the conditions of attraction and repulsion from the update equations (10)-(13). The following proposition characterizes the contraction of distance between the pair  $y_i^t$  and  $y_j^t$  of a positive edge:

**Proposition 4.1.** *The update Eqs. (10) and (11) provide a contraction of distance ( $\|y_i^{t+1} - y_j^{t+1}\| < \|y_i^t - y_j^t\|$ ) if  $-1 < \lambda f_a < 0$ .*

*Proof.* We subtract Eq. (10) from Eq. (11) and take a norm:

$$\|y_i^{t+1} - y_j^{t+1}\| = |1 + 2\lambda f_a| \|y_i^t - y_j^t\|. \quad (14)$$

This distance contracts as long as  $|1 + 2\lambda f_a| < 1$ , i.e., provided

$$-1 < \lambda f_a < 0, \quad (15)$$

□

Here,  $\lambda f_a$  works as the effective attraction shape. In most cases, however,  $f_a$  alone is enough to draw meaningful conclusions about the embeddings.

For a negative edge, the following proposition characterizes the expansion of the distance between the pair  $y_i^t$  and  $y_j^t$ :

**Proposition 4.2.** *The update Eqs. (12) and (13) provide an expansion of distance ( $\|y_i^{t+1} - y_j^{t+1}\| > \|y_i^t - y_j^t\|$ ) if  $f_r > 0$ .*

*Proof.* We subtract Eq. (12) from Eq. (13) and take a norm:

$$\|y_i^{t+1} - y_j^{t+1}\| = |1 + \lambda f_r| \|y_i^t - y_j^t\|. \quad (16)$$



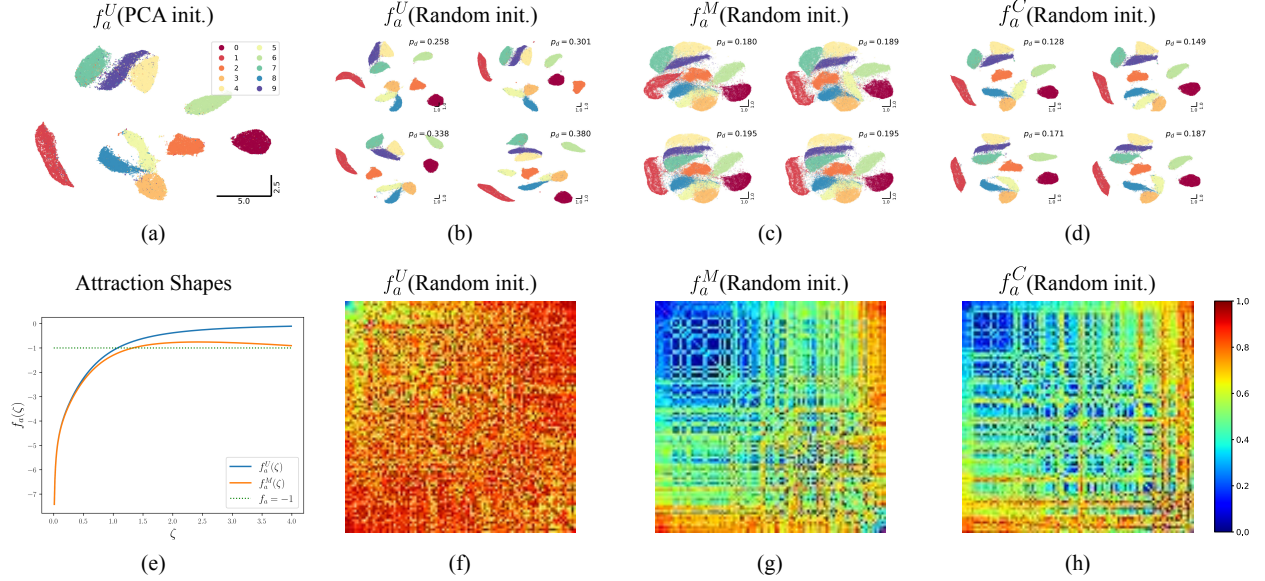


Figure 2: Effect of random initialization on different attraction shapes for the MNIST dataset. (a) Mapping using PCA. (b-d) Four mappings with the lowest Procrustes distance ( $p_d$ ) from the embedding in (a) for (b) UMAP, (c) modified, and (d) composite attraction shapes. (e) Default UMAP and modified attraction shapes. (f-h) Procrustes matrices from 100 runs of (f) UMAP ( $0.78 \pm 0.13$ ), (g) modified ( $0.49 \pm 0.21$ ), and (h) composite attraction ( $0.50 \pm 0.20$ ) shapes. The diagonal  $(i, i)$  entries of the Procrustes matrix are sorted by Procrustes distance ( $p_d$ ) from (a), and the off-diagonal,  $(i, j)$ , entries correspond to  $p_d$  between  $i^{th}$  and  $j^{th}$  mapping. The matrices and (mean  $p_d \pm \text{std}$ ) values show that UMAP's embeddings are not self-similar, while the modified and composite attraction shapes encourage scale-invariant structure.

This distance increases when  $|1 + \lambda f_r| > 1$ , i.e.,

$$\lambda f_r < -2 \text{ or } f_r > 0. \quad (17)$$

From the definition of  $f_r$ , the latter suffices.  $\square$

Note that the inclusion of a symmetric term  $-\lambda f_r(\zeta)(y_i^t - y_j^t)$  in Eq. (13) does not alter the conclusion presented in this proposition.

Figure 1 (a) shows the effect of different values of  $f_a < 0$  and  $f_r > 0$  on two points. The latter shape is straightforward, as any positive value increases the distance. The former is much more subtle, as  $f_a$  encodes both attractive and repulsive dynamics. For  $f_a \in (-1.0, 0)$ , the distance decreases, with a sign flip at the value  $f_a = -0.5$  of maximum attraction (coincident points). Any value lower than  $-1.0$  causes the distance to increase.

## 5 Analysis of UMAP in terms of Attraction and Repulsion Shape

Using the gradient decomposition and the distance form (4), the attraction and repulsion shapes are given by

$$f_a^U(\zeta) = -\frac{2ab\zeta^{2(b-1)}}{1 + a\zeta^{2b}} \quad (18)$$

and

$$f_r^U(\zeta) = \frac{2b}{\zeta^{2b}(1 + a\zeta^{2b})}, \quad (19)$$

respectively. This section focuses on the default shapes of UMAP, controlled primarily by the parameters  $a$  and  $b$ , and discusses the insights learned by perturbing them. The discussion below is generally valid for  $b \leq 1$ , where the attraction shape is strictly increasing and thus invertible. (For the derivations, see Appendix A)

Figure 1 (b) shows the default attraction shape of UMAP ( $a = 1.58, b = 0.87$ ). It becomes unbounded (approaches  $\infty$ ) as  $\zeta \rightarrow 0$ . As predicted by Proposition 4.1, the transition from contraction to expansion occurs when  $\lambda f_a^U$

crosses  $-1$  as  $\zeta$  approaches 0. Since the attraction shape is invertible, we can identify the distance at this transition,  $\zeta_{-1} = (\lambda f_a^U)^{-1}(-1)$ , as the minimum distance for contraction due to attractive updates. Effectively,  $\zeta > \zeta_{-1}$  causes contraction, and  $0 < \zeta < \zeta_{-1}$  causes expansion, contradicting the intuition that attractive updates consistently bring points closer together.

If  $\zeta_{-1}$  is high, neighboring points oscillate between contraction and expansion, and the clusters appear fuzzy. For the sharpest boundaries, then, the goal of optimization can be recast as one of achieving the limit  $\zeta_{-1} \rightarrow 0$ . As a result, UMAP’s learning rate schedule requires annealing to zero (Figs. 1 (c,d)). We explore this point further in Section 6, where we comment on the stability of the algorithm and compare it to NEG- $t$ -SNE for  $a = b = 1$ , and in Appendix B, where we discuss using a constant learning rate in UMAP.

On the other hand, the repulsion shape (Eq. 19) is always positive and satisfies Proposition 4.2.  $f_r^U$  approaches 0 as  $\zeta \rightarrow \infty$  and approaches  $\infty$  as  $\zeta \rightarrow 0$  (Fig. 1 (e)). We consider further the implications of repulsion shapes in Section 5.2.

### 5.1 Improving UMAP’s Consistency under Random Initialization

The consistency of UMAP embeddings depends on proper initialization [36, 12]. Typically, principal component analysis (PCA) of the data or spectral decomposition of the high-dimensional graph initializes the embedding, producing consistent mappings despite various sources of stochasticities. If randomly initialized, clusters often fail to form or form in a random orientation each time the algorithm executes. If the initial distance between two points (nearest neighbors in high dimension) is large, then the attractive forces become too low to bring them closer. Known as near-sightedness [12], this phenomenon is evident in the attraction shape, where  $f_a^U$  diminishes towards zero as the distance increases.

One can induce “far-sightedness” in the mapping by increasing attraction for large distances, facilitating faraway neighbors to come closer. To test this hypothesis, we modify the attraction shape of UMAP to increase the attractive force:

$$f_a^M = f_a^U - \beta\zeta, \quad (20)$$

where  $\beta$  is a parameter that regulates the strength of the added term. (We used  $\beta = 0.2$ , Fig. 2 (e).) In addition to attracting pairs at faraway distances, this technique enables intermixing of points that help under random initialization. In (20), we chose the simplest linear correction; other functions, such as  $\log \zeta$  or  $\zeta^p$  ( $p \in \mathbb{R}_{\geq 0}$ ), may also be suitable.

We also consider a composite attraction shape:

$$f_a^C = \begin{cases} f_a^M, & \text{epoch} \leq 100 \\ f_a^U, & \text{otherwise} \end{cases}. \quad (21)$$

The composite shape attempts to remove any distortions introduced by  $f_a^M$  by reverting to the original UMAP. Below, we discuss the effects these modified and composite attraction shapes have on DR from random initialization.

We first created a PCA-initialized embedding of the MNIST dataset Figure 2 (a). Then, we produced embeddings using random initialization (Gaussian) for each shape and repeated the experiment 100 times. To quantify the results, we use Procrustes analysis [37] that aligns two point clouds under scaling, translation, rotation, and reflection (for details, see Appendix D). Here, we align the randomly initialized embeddings to that of the PCA-initialized one and characterize their separation using the Procrustes distance ( $p_d$ ). Figure 2 (b) shows four embeddings with the lowest  $p_d$ . While the cluster shapes are consistent, their placements are not. Outputs from the modified and composite attraction shapes (Figs. 2 (c) and (d), respectively) show improved consistency of cluster placements.

To quantify the placements further, we consider the Procrustes matrix: the diagonal of the matrix is sorted by  $p_d$  from the PCA-initialized mapping, and the off-diagonal values are  $p_d$  between two randomly initialized mappings. This quantification is analogous to the similarity matrix [38]. The embeddings due to the default UMAP attraction shape are not similar to each other (Fig. 2 (f)), but the modified (Fig. 2 (g)) and composite (Fig. 2 (h)) shapes show strong similarity to each other. This indicates that UMAP encodes a unique structure, regardless of the initialization. However, attaining that structure in the low dimension may fall short due to small attraction at longer distances.

### 5.2 Increasing Compactness of Clusters

The primary controllable parameter influencing cluster formation in UMAP is the minimum distance parameter  $m_d$  (through Eq. 5). However, varying  $m_d$  restricts the exploration of different values of  $a$  and  $b$  (Fig. 3 (a)). Thus, reducing  $m_d$  often results in embeddings that do not provide additional benefit (Figs. 3 (b-d)). The key factor is the limited influence of varying  $m_d$  on the repulsion shape (Fig. 3 (e)). To overcome this, we modify the repulsion shape by adding

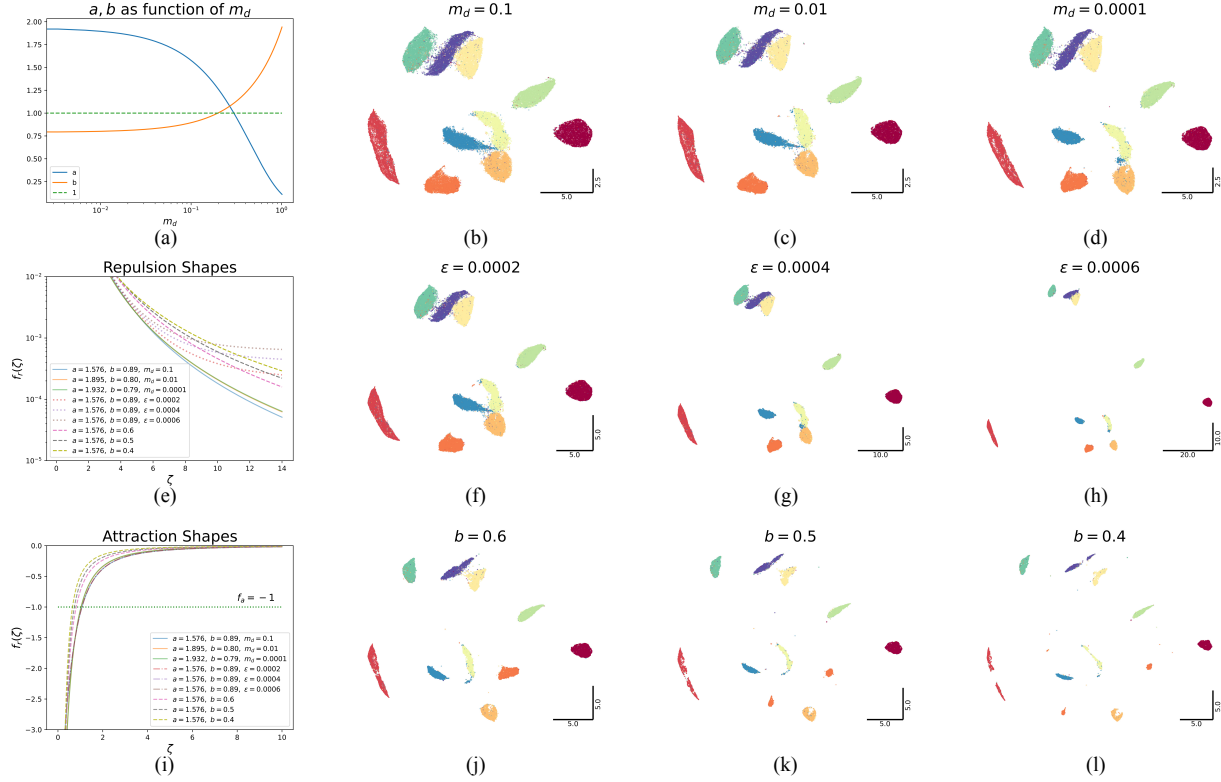


Figure 3: Control of inter-cluster distances on the MNIST dataset. (a) Computing  $a, b$  by varying the low-dimensional distance  $m_d$  restricts exploration. (b-d) UMAP output by setting  $m_d$  to 0.1, 0.01, and 0.0001, respectively, shows little improvement in compactness of clusters. (e) Repulsion shapes for different parameters. (f-h) Increasing repulsion by adding a small positive value ( $\epsilon$ ) to the repulsion shape increases inter-cluster distance. (i) Attraction shapes by varying parameters. (j-l) Increasing repulsion by explicitly varying  $b$  results in more compact clusters and forms new ones that were absent otherwise.

a small positive value ( $\epsilon$ ):

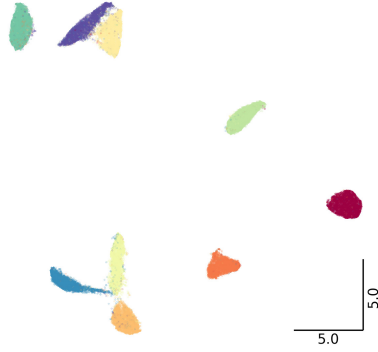
$$f_r^M = f_r^U + \epsilon, \quad (22)$$

while keeping the values of  $a$  and  $b$  constant. Figs. 3 (f-h) show that as  $\epsilon$  increases, the inter-cluster distances also increase. However, the clustering properties exhibit similarity to those obtained by varying  $m_d$ . The parameter  $\epsilon$  keeps the attraction shape unaffected, and varying  $m_d$  effectively traces similar attraction shapes (Fig. 3 (i)), suggesting cluster formation is governed predominantly by attraction.

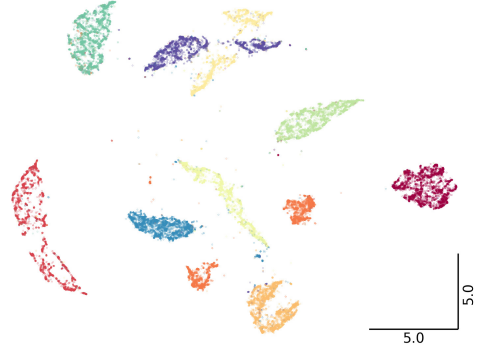
To confirm, we explicitly varied the values of  $a$  and  $b$ . Decreasing  $a$  increases repulsion, but it decreases attraction at a faster rate (causing near-sightedness). On the other hand, decreasing  $b$  gives better control (Figs. 3 (e,i)). Figures 3 (j-l) show increasing inter-cluster distance and breaking up of previous clusters by varying  $b$  to 0.6, 0.5, and 0.4, respectively. These values result in a higher repulsion than by varying  $m_d$  but lower than that by varying  $\epsilon$  (for smaller distances shown in Fig. 3(e)).

To resolve the action of  $b$ , we change either the attraction shape or the repulsion shape individually while leaving the other shape at the default value (Fig. 4). The default attraction is unable to show new structures or clusters in the embedding, but the increased repulsion ( $b = 0.4$ ) gives smaller clusters than the original UMAP (Fig. 4 (a)). On the other hand, when the attraction increases by setting  $b = 0.4$  with the default repulsion, the embedding shows additional structures within each cluster (Fig. 4 (b)). Some of the older clusters even separate into smaller ones. This shows that attraction causes cluster formation, while repulsion makes the clusters more compact (depending on the repulsion shape, it does this either by making smaller clusters or increasing inter-cluster distance).

We show in appendix F.3 that LocalMAP embeddings also exploit this interplay of attraction and repulsion to separate the clusters.

$f_a^U$ : Default,  $f_r^U$ :  $b = 0.4$ 

(a)

 $f_a^U$ :  $b = 0.4$ ,  $f_r^U$ : Default

(b)

Figure 4: Embedding of the MNIST dataset with (a) default attraction shape but repulsion shape with  $b = 0.4$  and (b) default repulsion shape but attraction shape with  $b = 0.4$ . The former shows the same clusters of default UMAP with increased compactness. The latter develops new structures within clusters and forms new clusters.

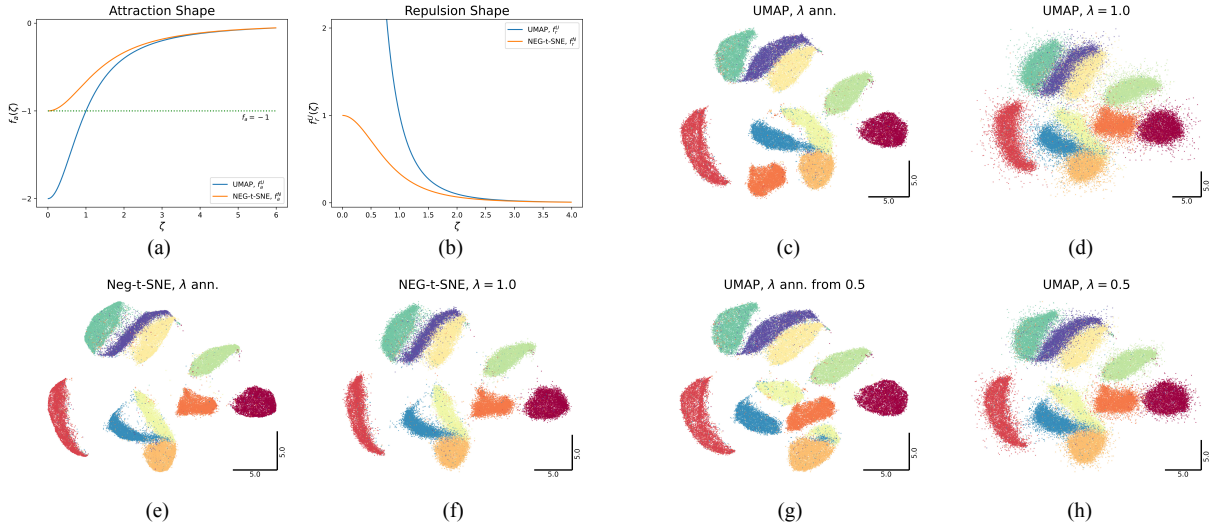


Figure 5: Sensitivity of UMAP and NEG- $t$ -SNE to learning rate on the MNIST dataset. (a) Attraction and (b) repulsion shapes for UMAP ( $a = 1$ ,  $b = 1$ ) and NEG- $t$ -SNE. (c,d) UMAP is very sensitive to the learning rate  $\lambda$ , as  $f_a^U < -1$  as the separation distance  $\zeta$  decreases. Thus, without annealing, the clusters become fuzzy. (e,f) NEG- $t$ -SNE is less sensitive to  $\lambda$  as  $f_a^N \in [-1, 0]$  always, and the clusters are thus less fuzzy even when not annealed. (g,h) Confining  $f_a^U$  to  $[-1, 0]$  by setting  $\lambda = 0.5$  shows less sensitivity to  $\lambda$ .

## 6 Comparison to NEG- $t$ -SNE

Setting  $a$  and  $b$  to 1 is common for various dimensionality reduction algorithms. Recently, Damrich et al. [27] explored this primarily through numerical stability. Here, we provide a deeper explanation using both attraction and repulsion shapes. Additionally, we explore the connection to NEG- $t$ -SNE by examining sensitivity to learning rate, in addition to numerical stability.

With  $a = 1$  and  $b = 1$ , the attraction and repulsion shapes of UMAP are given by  $f_a^U = -2/(1 + \zeta^2)$  and  $f_r^U = 2/(\zeta^2(1 + \zeta^2))$ , respectively. The attraction shape is bounded within  $[-2, 0]$ , with  $f_a^U(0) = -2$  (Fig. 5 (a)). While the repulsion shape remains essentially unchanged (unbounded as  $\zeta \rightarrow 0$ , Fig. 5 (b)). Since  $f_a^U < -1$  as  $\zeta \rightarrow 0$ , according to Proposition 4.1 and the discussion provided in Section 5, this unity case still requires learning rate annealing.

Figures 5 (c) and (d) show the effect of annealing and constant  $\lambda = 1.0$ , respectively. The clusters appear fuzzy for a fixed learning rate.

Damrich et al. [27] compared UMAP’s negative sampling loss function from the perspective of contrastive embedding (CE) and concluded that the effective kernel of UMAP is  $1/\zeta^2$ . Under the CE framework, the authors introduced NEG-*t*-SNE by changing the kernel to  $1/(1 + \zeta^2)$ . In the UMAP formalism, this results in the low-dimensional affinity function  $q_{ij}^N = 1/(2 + \zeta^2)$ . Consequently, the attraction and repulsion shapes are  $f_a^N = -2/(2 + \zeta^2)$ , and  $f_r^N = 2/((1 + \zeta^2)(2 + \zeta^2))$ , respectively. The attraction shape is bounded within  $[-1, 0]$  and satisfies Proposition 4.1. Any  $\lambda \in [0, 1]$  would cause contraction and avoid oscillation of expansion and contraction. Thus, NEG-*t*-SNE is less sensitive to learning rate annealing, and the clusters appear less fuzzy even for constant  $\lambda = 1.0$  (Figs. 5 (e,f)). Moreover, the repulsion shape of NEG-*t*-SNE is also bounded within  $[0, 1]$  and does not approach infinity as  $\zeta \rightarrow 0$ . While Damrich et al. [27] used the bounded repulsive forces of NEG-*t*-SNE and unbounded ones of UMAP to explain this disparity, our analysis shows that the attraction shape and Proposition 4.1 provide a better explanation.

This discussion suggests that constraining  $f_a^U$  within  $[-1, 0]$  can potentially result in less fuzzy clusters for fixed  $\lambda$ . A straightforward way to achieve this is to initialize  $\lambda$  to 0.5, which satisfies Proposition 4.1 for all  $\zeta$ . The resulting embeddings, shown in Figs. 5 (g) and (h), confirm that clusters are similar to those of NEG-*t*-SNE’s.

Next, we introduce the parameters  $a$  and  $b$  into NEG-*t*-SNE. The affinity function becomes  $q_{ij}^N = 1/(2 + a\zeta^{2b})$ , and the attraction and repulsion shapes become

$$f_a^N = -\frac{2ab\zeta^{2(b-1)}}{2 + a\zeta^{2b}}, \quad (23)$$

and

$$f_r^N = \frac{2ab\zeta^{2(b-1)}}{(1 + a\zeta^{2b})(2 + a\zeta^{2b})}, \quad (24)$$

respectively. For  $0 < b < 1$ , both shapes become unbounded as  $\zeta \rightarrow 0$ . Thus, NEG-*t*-SNE will face similar numerical challenges to UMAP if  $a$  and  $b$  vary, and corresponding limitations carry over. One notable distinction is that, compared to UMAP, the attraction shape attains a lower minimum distance ( $\zeta_{-1}$ ) for the attraction. While this may enhance cluster formation, it approaches zero faster (near-sightedness as distance increases), potentially diminishing its effectiveness for attraction over longer distances.

## 7 Discussion and Conclusion

In this work, we studied the relationship of attractive and repulsive forces to cluster formation. While it is known that attractive forces bring similar points closer together and repulsive forces push dissimilar samples further away, the exact mechanisms of such forces was not well studied. Here, we demystified much of dynamics underlying cluster formation. While we focused on UMAP and NEG-*t*-SNE, the results are general to dimensionality reduction (some other algorithms are discussed in the Appendix F).

We considered attraction and repulsion coefficients as functions and contextualized the attraction and repulsion shapes. Characterizing these shapes (Propositions 4.1 and 4.2) revealed a counterintuitive result: the attractive forces of UMAP gave repulsion (expansion of distance) for shorter distances (Fig. 1 (b)), i.e. instead of bringing neighboring points closer together, it pushes them away. We conclude that UMAP’s learning rate schedule alleviates this phenomenon.

We also studied the initialization of the low-dimensional embedding. Similar points starting further apart experience low attraction and never contract well enough. Our formalism provides a way to influence attraction at larger distances by adding additional terms to the attraction shape. This modification resulted in outputs that are more consistent under random initialization. This gives confidence that UMAP encodes a unique structure, with numerical tricks merely helping to achieve it faster.

Analyzing the repulsion shape revealed that higher repulsion causes a larger inter-cluster distance. To this end, we added a small positive value to the shape, giving a higher repulsion that is not achievable by traditional means of varying the minimum distance parameter  $m_d$ . Alternatively, varying the parameter  $b$  in the low-dimensional mapping enhances cluster formation through improved interplay of attraction and repulsion.

Finally, we explored the relation between NEG-*t*-SNE and UMAP. For the particular case  $a = 1$  and  $b = 1$ , the primary difference is that NEG-*t*-SNE in its default form provides bounded attraction ( $\in [-1, 0]$ ) and repulsion ( $\in [0, 1]$ ) shapes. Thus, both propositions are satisfied regardless of the learning rate. As a result, the method shows less sensitivity to a fixed learning rate ( $\in [0, 1]$ ). Varying  $a$  and  $b$  in NEG-*t*-SNE introduces the same numerical challenges as UMAP.

These insights into the underlying attraction-repulsion dynamics offer new tools for optimizing dimensionality reduction algorithms. More generally, the relation of DR to contrastive learning [39, 31] suggests that our approach can improve representation learning through contrast as well. Overall, our work will make embeddings and their interpretations more informed, more consistent, and more reliable.

## Acknowledgement

This work was supported by AFOSR grant FA9550-21-1-0317 and the Schmidt DataX Fund at Princeton University, made possible through a major gift from the Schmidt Futures Foundation. Mohammad Tariqul Islam is supported by MIT-Novo Nordisk Artificial Intelligence Fellowship.

## Software and Data

All the data used in this paper are publicly available. The MNIST dataset is available at <https://yann.lecun.com/exdb/mnist/>. Fashion-MNIST is available at <https://github.com/zalandoresearch/fashion-mnist>. Single-cell transcriptomes data is available at <https://github.com/biolab/tsne-embedding>. Codes for reproducing the results are available at [https://github.com/tariqul-islam/explaining\\_neighbor\\_embedding](https://github.com/tariqul-islam/explaining_neighbor_embedding).

## Impact Statement

This work provides a fresh perspective on nonlinear dimensionality reduction by analyzing the gradients and forming attraction-repulsion shapes as independent constructs. Our analysis shows that many heuristics of DR algorithms can be explained using these shapes. Moreover, transformations of these shapes extends the range of the algorithms beyond their conventional boundaries. Our work will be useful for applications in computational biology, medical image analysis, and visual search technology.

## References

- [1] Laurens van der Maaten and Geoffrey Hinton. Visualizing data using t-sne. *Journal of machine learning research*, 9(Nov):2579–2605, 2008.
- [2] Leland McInnes, John Healy, and James Melville. UMAP: Uniform manifold approximation and projection for dimension reduction. *arXiv preprint arXiv:1802.03426*, 2018.
- [3] Etienne Becht, Leland McInnes, John Healy, Charles-Antoine Dutertre, Immanuel WH Kwok, Lai Guan Ng, Florent Ginhoux, and Evan W Newell. Dimensionality reduction for visualizing single-cell data using umap. *Nature biotechnology*, 37(1):38–44, 2019.
- [4] Jason Fleischer and Mohammad Tariqul Islam. Late breaking abstract-identifying and phenotyping COVID-19 patients using machine learning on chest x-rays. *European Respiratory Journal*, 2020.
- [5] Shu-Kai S Fan, Du-Ming Tsai, Chih-Hung Jen, Chia-Yu Hsu, Fei He, and Li-Ting Juan. Data visualization of anomaly detection in semiconductor processing tools. *IEEE Transactions on Semiconductor Manufacturing*, 35(2):186–197, 2021.
- [6] Rita González-Márquez, Luca Schmidt, Benjamin M Schmidt, Philipp Berens, and Dmitry Kobak. The landscape of biomedical research. *Patterns*, 2024.
- [7] Mahsun Altin and Altan Cakir. Exploring the influence of dimensionality reduction on anomaly detection performance in multivariate time series. *IEEE Access*, 2024.
- [8] Minyoung Huh, Brian Cheung, Tongzhou Wang, and Phillip Isola. The platonic representation hypothesis. *arXiv preprint arXiv:2405.07987*, 2024.
- [9] Mohammad Tariqul Islam and Jason W Fleischer. Outlier detection in large radiological datasets using umap. In *International Workshop on Topology-and Graph-Informed Imaging Informatics*, pages 111–121. Springer, 2024.
- [10] Ehsan Amid and Manfred K Warmuth. TriMap: Large-scale dimensionality reduction using triplets. *arXiv preprint arXiv:1910.00204*, 2019.
- [11] Akshay Agrawal, Alnur Ali, Stephen Boyd, et al. Minimum-distortion embedding. *Foundations and Trends® in Machine Learning*, 14(3):211–378, 2021.

- [12] Yingfan Wang, Haiyang Huang, Cynthia Rudin, and Yaron Shaposhnik. Understanding how dimension reduction tools work: an empirical approach to deciphering t-SNE, UMAP, TriMAP, and PaCMAP for data visualization. *The Journal of Machine Learning Research*, 22(1):9129–9201, 2021.
- [13] Ashwin Narayan, Bonnie Berger, and Hyunghoon Cho. Assessing single-cell transcriptomic variability through density-preserving data visualization. *Nature Biotechnology*, 39(6):765–774, 2021.
- [14] Yang Yang, Hongjian Sun, Jialei Gong, Yali Du, and Di Yu. Interpretable dimensionality reduction by feature preserving manifold approximation and projection. *arXiv preprint arXiv:2211.09321*, 2022.
- [15] Yingfan Wang, Yiyang Sun, Haiyang Huang, and Cynthia Rudin. Dimension reduction with locally adjusted graphs. In *Thirty-Ninth AAAI Conference on Artificial Intelligence*, 2025.
- [16] Tara Chari and Lior Pachter. The specious art of single-cell genomics. *PLOS Computational Biology*, 19(8):e1011288, 2023.
- [17] Geoffrey Hinton and Sam T Roweis. Stochastic neighbor embedding. In *Advances in Neural Information Processing Systems*, volume 15, pages 833–840, 2002.
- [18] Sam T Roweis and Lawrence K Saul. Nonlinear dimensionality reduction by locally linear embedding. *science*, 290(5500):2323–2326, 2000.
- [19] Mikhail Belkin and Partha Niyogi. Laplacian eigenmaps and spectral techniques for embedding and clustering. In *Advances in neural information processing systems*, pages 585–591, 2002.
- [20] Jian Tang, Jingzhou Liu, Ming Zhang, and Qiaozhu Mei. Visualizing large-scale and high-dimensional data. In *Proceedings of the 25th international conference on world wide web*, pages 287–297, 2016.
- [21] Uri Shaham and Stefan Steinerberger. Stochastic neighbor embedding separates well-separated clusters. *arXiv preprint arXiv:1702.02670*, 2017.
- [22] George C Linderman and Stefan Steinerberger. Clustering with t-SNE, provably. *SIAM Journal on Mathematics of Data Science*, 1(2):313–332, 2019.
- [23] Sanjeev Arora, Wei Hu, and Praveesh K Kothari. An analysis of the t-sne algorithm for data visualization. In *Conference On Learning Theory*, pages 1455–1462. PMLR, 2018.
- [24] T Tony Cai and Rong Ma. Theoretical foundations of t-sne for visualizing high-dimensional clustered data. *Journal of Machine Learning Research*, 23(301):1–54, 2022.
- [25] George C Linderman and Stefan Steinerberger. Dimensionality reduction via dynamical systems: The case of t-sne. *SIAM Review*, 64(1):153–178, 2022.
- [26] Jan Niklas Böhm, Philipp Berens, and Dmitry Kobak. Attraction-repulsion spectrum in neighbor embeddings. *The Journal of Machine Learning Research*, 23(1):4118–4149, 2022.
- [27] Sebastian Damrich, Niklas Böhm, Fred A Hamprecht, and Dmitry Kobak. From t-SNE to UMAP with contrastive learning. In *The Eleventh International Conference on Learning Representations*, 2023.
- [28] Andrew Draganov, Jakob Jørgensen, Katrine Scheel, Davide Mottin, Ira Assent, Tyrus Berry, and Cigdem Aslay. ActUp: Analyzing and consolidating tSNE and UMAP. In *Proceedings of the Thirty-Second International Joint Conference on Artificial Intelligence, IJCAI-23*, pages 3651–3658, 8 2023.
- [29] Aditya Ravuri, Francisco Vargas, Vidhi Lalchand, and Neil D Lawrence. Dimensionality reduction as probabilistic inference. In *ICML 2023 Workshop on Structured Probabilistic Inference & Generative Modeling*, 2023.
- [30] Mathieu Jacomy, Tommaso Venturini, Sebastien Heymann, and Mathieu Bastian. Forceatlas2, a continuous graph layout algorithm for handy network visualization designed for the gephi software. *PloS one*, 9(6):e98679, 2014.
- [31] Tianyang Hu, Zhili Liu, Fengwei Zhou, Wenjia Wang, and Weiran Huang. Your contrastive learning is secretly doing stochastic neighbor embedding. In *The Eleventh International Conference on Learning Representations*, 2023.
- [32] Aditya Ravuri and Neil D Lawrence. Towards one model for classical dimensionality reduction: A probabilistic perspective on umap and t-sne. *arXiv preprint arXiv:2405.17412*, 2024.
- [33] Andrew Draganov and Simon Dohn. Relating tsne and umap to classical dimensionality reduction. *arXiv e-prints*, pages arXiv–2306, 2023.
- [34] Alexander Kolpakov and Aidan Rocke. The information geometry of umap. *arXiv preprint arXiv:2309.01237*, 2023.
- [35] Tomas Mikolov, Ilya Sutskever, Kai Chen, Greg S Corrado, and Jeff Dean. Distributed representations of words and phrases and their compositionality. In *Advances in neural information processing systems*, pages 3111–3119, 2013.

- [36] Dmitry Kobak and George C Linderman. Initialization is critical for preserving global data structure in both t-sne and umap. *Nature biotechnology*, 39(2):156–157, 2021.
- [37] John C Gower. Generalized procrustes analysis. *Psychometrika*, 40:33–51, 1975.
- [38] Jonathan Foote. Visualizing music and audio using self-similarity. In *Proceedings of the seventh ACM international conference on Multimedia (Part 1)*, pages 77–80, 1999.
- [39] Sebastian Damrich and Fred A Hamprecht. On UMAP’s true loss function. *Advances in Neural Information Processing Systems*, 34:5798–5809, 2021.
- [40] Yu Gu, Robert Tinn, Hao Cheng, Michael Lucas, Naoto Usuyama, Xiaodong Liu, Tristan Naumann, Jianfeng Gao, and Hoifung Poon. Domain-specific language model pretraining for biomedical natural language processing. *ACM Transactions on Computing for Healthcare (HEALTH)*, 3(1):1–23, 2021.
- [41] Mohammad Tariqul Islam and Jason W Fleischer. Manifold-aligned neighbor embedding. In *ICLR 2022 Workshop on Geometrical and Topological Representation Learning*, 2022.
- [42] Nikita Kotlov, Kirill Shaposhnikov, Cagdas Tazearslan, Madison Chasse, Artur Baisangurov, Svetlana Podsvirova, Dawn Fernandez, Mary Abdou, Leznath Kaneunyenye, Kelley Morgan, et al. Procrustes is a machine-learning approach that removes cross-platform batch effects from clinical rna sequencing data. *Communications Biology*, 7(1):392, 2024.
- [43] Han Xiao, Kashif Rasul, and Roland Vollgraf. Fashion-MNIST: A novel image dataset for benchmarking machine learning algorithms. 2017.
- [44] Evan Z Macosko, Anindita Basu, Rahul Satija, James Nemesh, Karthik Shekhar, Melissa Goldman, Itay Tirosh, Allison R Bialas, Nolan Kamitaki, Emily M Martersteck, et al. Highly parallel genome-wide expression profiling of individual cells using nanoliter droplets. *Cell*, 161(5):1202–1214, 2015.
- [45] Laurens Van der Maaten and Geoffrey Hinton. Visualizing data using t-sne. *Journal of machine learning research*, 9(11), 2008.
- [46] Robert A Jacobs. Increased rates of convergence through learning rate adaptation. *Neural networks*, 1(4):295–307, 1988.
- [47] Diederik P Kingma and Jimmy Ba. Adam: A method for stochastic optimization. In *International Conference on Learning Representations*, 2015.
- [48] Pavlin Gregor Policar, Martin Strazar, and Blaz Zupan. opensne: a modular python library for t-sne dimensionality reduction and embedding. *BioRxiv*, page 731877, 2019.
- [49] Siu Kwan Lam, Antoine Pitrou, and Stanley Seibert. Numba: A llvm-based python jit compiler. In *Proceedings of the Second Workshop on the LLVM Compiler Infrastructure in HPC*, pages 1–6, 2015.
- [50] F. Pedregosa, G. Varoquaux, A. Gramfort, V. Michel, B. Thirion, O. Grisel, M. Blondel, P. Prettenhofer, R. Weiss, V. Dubourg, J. Vanderplas, A. Passos, D. Cournapeau, M. Brucher, M. Perrot, and E. Duchesnay. Scikit-learn: Machine learning in Python. *Journal of Machine Learning Research*, 12:2825–2830, 2011.
- [51] Pauli Virtanen, Ralf Gommers, Travis E. Oliphant, Matt Haberland, Tyler Reddy, David Cournapeau, Evgeni Burovski, Pearu Peterson, Warren Weckesser, Jonathan Bright, Stéfan J. van der Walt, Matthew Brett, Joshua Wilson, K. Jarrod Millman, Nikolay Mayorov, Andrew R. J. Nelson, Eric Jones, Robert Kern, Eric Larson, C J Carey, İlhan Polat, Yu Feng, Eric W. Moore, Jake VanderPlas, Denis Laxalde, Josef Perktold, Robert Cimrman, Ian Henriksen, E. A. Quintero, Charles R. Harris, Anne M. Archibald, Antônio H. Ribeiro, Fabian Pedregosa, Paul van Mulbregt, and SciPy 1.0 Contributors. SciPy 1.0: Fundamental Algorithms for Scientific Computing in Python. *Nature Methods*, 17:261–272, 2020.



## Appendix

In Appendix A, we provide necessary derivations regarding attraction and repulsion shapes. In Appendix B we explore using a constant learning rate following our discussion in the main text. Then, in Appendix C, we discuss the implications of improved attraction and repulsion on large language model embeddings. We formally define Procrustes distance and matrix in Appendix D. We explore few additional datasets in Appendix E. After that, in Appendix F, we explore alternate dimensionality reduction methods. Finally, we provide implementation details in Appendix G.

### A Derivations

#### Attraction Shape:

We use a general form of the low-dimensional affinity function, i.e.,  $q_{ij} = (\gamma + a\|y_i - y_j\|_2^{2b})^{-1}$ , to derive the attraction shape. It reduces to UMAP for  $\gamma = 1$  and to NEG- $t$ -SNE for  $\gamma = 2$ . The attractive force is given by

$$\begin{aligned}\nabla_{y_i} \log q_{ij} &= -\nabla_{y_i} \log (\gamma + a(\|y_i - y_j\|_2^2)^b) \\ &= -\frac{1}{\gamma + a(\|y_i - y_j\|_2^2)^b} \nabla_{y_i} (\gamma + a(\|y_i - y_j\|_2^2)^b) \\ &= -\frac{1}{\gamma + a(\|y_i - y_j\|_2^2)^b} ab(\|y_i - y_j\|_2^2)^{b-1} \nabla_{y_i} \|y_i - y_j\|_2^2 \\ &= -\frac{2ab(\|y_i - y_j\|_2^2)^{b-1}}{\gamma + a(\|y_i - y_j\|_2^2)^b} (y_i - y_j).\end{aligned}\tag{25}$$

Defining  $\zeta = \|y_i - y_j\|_2$ , the first term gives the attraction shape as:

$$f_a(\zeta) = -\frac{2ab\zeta^{2(b-1)}}{\gamma + a\zeta^{2b}}\tag{26}$$

#### Condition for strictly increasing $f_a^U$ :

Its behavior with distance can be characterized by computing the derivative of  $f_a^U$ :

$$\frac{df_a^U(\zeta)}{d\zeta} = -\frac{2ab\zeta^{2b-3}}{\gamma + a\zeta^{2b}} \left( (b-1) - \frac{ab\zeta^{2b}}{\gamma + a\zeta^{2b}} \right).\tag{27}$$

This leads to a strictly increasing condition ( $\frac{df_a^U}{d\zeta} > 0$ ),

$$g(\zeta, b, a) < 0,\tag{28}$$

where  $g(\zeta, b, a) = b - 1 - \frac{ab\zeta^{2b}}{\gamma + a\zeta^{2b}}$ . This inequality is valid as long as  $0 < b \leq 1$  (using the derivative and asymptotes of  $g$ ). Figure 6 shows values of  $g$  for different  $b$  and  $a$ . As  $b$  increases above 1, the inequality (28) no longer holds.

#### Repulsion Shape:

The repulsive force, using the general form of the low-dimensional affinity, is given by

$$\begin{aligned}\nabla_{y_i} \log (1 - q_{ij}) &= \nabla_{y_i} \log \left[ 1 - \frac{1}{\gamma + a(\|y_i - y_j\|_2^2)^b} \right] \\ &= \frac{\gamma + a(\|y_i - y_j\|_2^2)^b}{(\gamma - 1) + a(\|y_i - y_j\|_2^2)^b} \nabla_{y_i} \left[ 1 - \frac{1}{\gamma + a(\|y_i - y_j\|_2^2)^b} \right] \\ &= \frac{1}{\gamma - 1 + a(\|y_i - y_j\|_2^2)^b} \frac{ab(\|y_i - y_j\|_2^2)^{b-1}}{\gamma + a(\|y_i - y_j\|_2^2)^b} \nabla_{y_i} \|y_i - y_j\|_2^2 \\ &= \frac{2ab(\|y_i - y_j\|_2^2)^{b-1}}{(\gamma - 1 + a(\|y_i - y_j\|_2^2)^b)(\gamma + a(\|y_i - y_j\|_2^2)^b)} (y_i - y_j).\end{aligned}\tag{29}$$

The first term gives the repulsion shape as:

$$f_r(\zeta = \|y_i - y_j\|_2) = \frac{2ab\zeta^{2(b-1)}}{(\gamma - 1 + a\zeta^{2b})(\gamma + a\zeta^{2b})}.\tag{30}$$

Generally,  $f_r > 0$ .

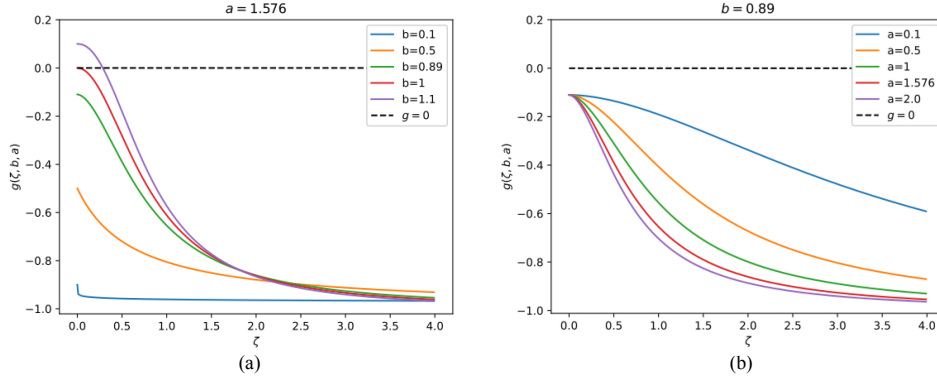


Figure 6: Values of  $g(\zeta, b, a)$  for (a)  $a$  fixed at 1.576 and (b)  $b$  fixed at 0.89.

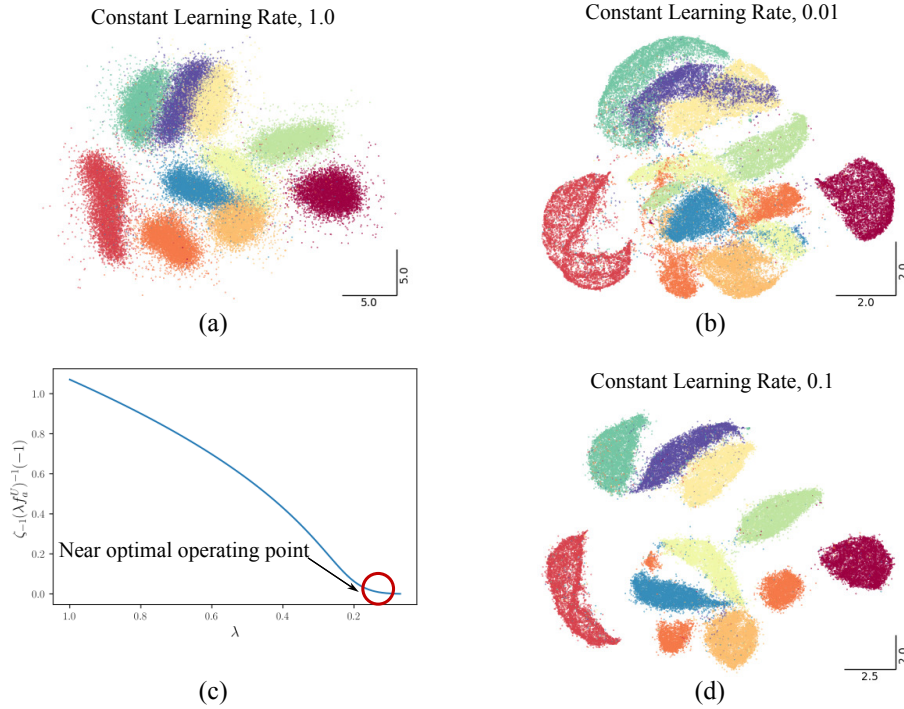


Figure 7: Effect of constant learning rate in embeddings. (a) When the learning rate is too high ( $\lambda = 1.0$ ), the embeddings are diffuse (because of the high value of  $\zeta_{-1}$ ). (b) When the learning rate is too low ( $\lambda = 0.01$ ), clusters don't form (the strengths of attraction and repulsion are too low). (c)  $\zeta_{-1}$  decreases nonlinearly as the learning rate decreases. The goal of the algorithm is to reduce  $\zeta_{-1}$  while keeping effective levels of attraction and repulsion. (d) Distinct and compact clusters form at a constant, near-optimal learning rate  $\lambda = 0.1$ .

## B More on UMAP's Learning Rate

As we discussed in Sections 5 and 6 of the main text, it is believed that UMAP requires learning rate annealing (Fig 7). To explain this, in Section 5, we defined the concept of minimum distance for contraction ( $\zeta_{-1}$ ) and established that reducing this value through learning rate annealing results in compact clusters. Later, in Section 6, we compared attraction shapes of UMAP (for  $a = 1.0$  and  $b = 1.0$ ) and Neg- $t$ -SNE and explained that Neg- $t$ -SNE can withstand a constant learning rate of 1.0 better than UMAP because it's attraction shape resides within  $[-1, 0]$  while UMAP's is within  $[-2, 0]$ . Following the same logic, we showed that UMAP can withstand a constant learning of 0.5 by making its attraction shape stay within  $[-1, 0]$  (Figs. 5(f,h)).

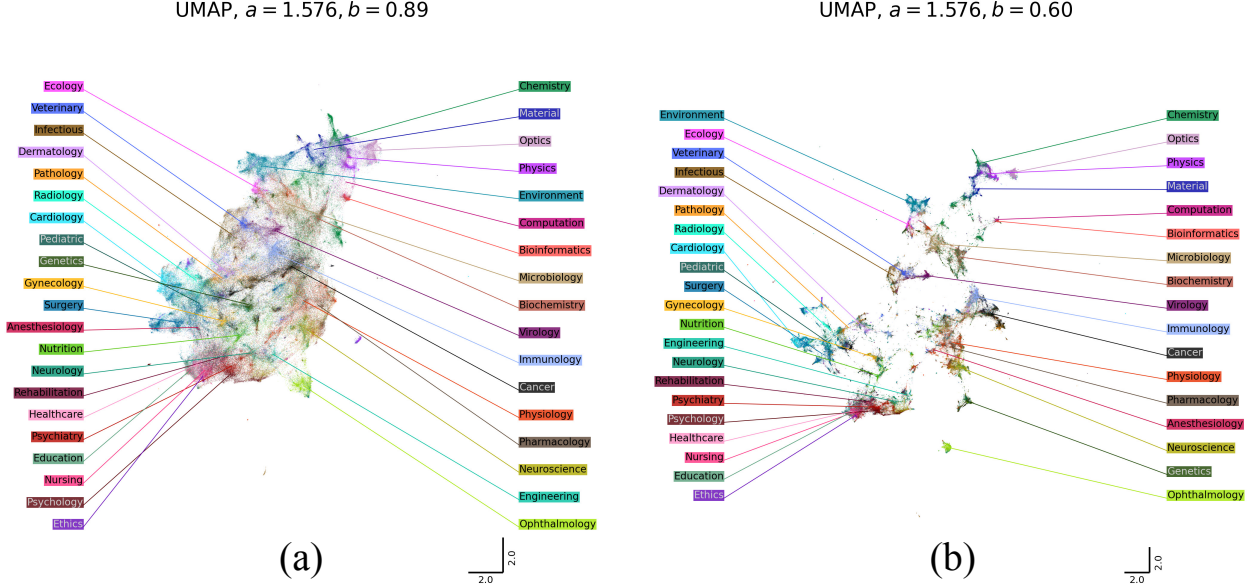


Figure 8: Visualization of 300K abstracts from the PubMed dataset. (a) Default UMAP ( $a = 1.576, b = 0.89$ ) shows labels overlapping each other in the mapping, but (b) UMAP with improved repulsion and attraction ( $a = 1.576, b = 0.60$ ) shows better cluster formation and non-overlapping labels. Both mappings are labeled for easier understanding.

However, the embeddings are still better if the learning rate anneals (for a wide range of parameters of  $a$  and  $b$ ). This is because the goal of the algorithm is to eventually reduce  $\zeta_{-1}$  to zero and it occurs when the learning rate reduces close to zero. Otherwise, the embedding becomes diffused (Fig 7(a)). On the other hand, if the learning rate is too low, to begin with, the strength of attraction and repulsion is too low, and thus no clear clusters can form (Fig 7(b)). By analyzing  $\zeta_{-1}$  vs  $\lambda$  curve (Fig 7(c)), we see that a near optimal point is  $\lambda = 0.1$  where the value of  $\zeta_{-1}$  is low with considerable attraction and repulsion strength. Setting the constant learning rate to 0.1, we obtain compact clusters with clear boundaries (Fig 7(d)).

## C Large Language Model Embedding

Increased attraction and repulsion often produce better embeddings. To show this, we randomly selected 300,000 samples of features using PubMedBERT [40] with known labels from the PubMed dataset [6]. The default UMAP provides a crowded structure where labels (colors) overlap (Fig. 8(a)). Without labels, one might be perplexed about the embeddings, as explicit clusters are absent. However, by adjusting  $b$  to 0.6 (as discussed in Section 5.2), we increase repulsion and simultaneously facilitate cluster formation through improved attraction. The mapping is explorable even without explicit labeling (Fig. 8(b)). The improvement of the embedding can be quantified by the k-NN accuracy ( $k = 10$ ). On a hold-out data of 10,000 points, k-NN accuracy has increased from 49.2% to 55.48% by reducing  $b$  to 0.6.

## D Procrustes Distance and Procrustes Matrix

The Procrustes distance [37] measures similarity between two point clouds  $\{x\}$  and  $\{y\}$  under linear transformations, viz. translation, scaling, and rotation. Operationally, we hold the former fixed and vary the latter until the two sets are in maximum alignment. Let  $\{y'\}$  be the transformation of  $\{y\}$  that achieves this objective. Then the Procrustes distance is given by

$$p_d(\{x\}, \{y\}) = \sqrt{\sum_k (x_k - y'_k)^2}. \quad (31)$$

The Procrustes distance is a linear measure that has proven useful in a variety of settings [2, 41, 42].

Here, we use the Procrustes distance to measure the consistency of embedding under random initialization. Let  $\{x\}_p$  be a reference embedding (using PCA initialization in our experiments), and  $X_r = \{\{x\}_i | i = 1, 2, 3, \dots, N\}$  be a set of

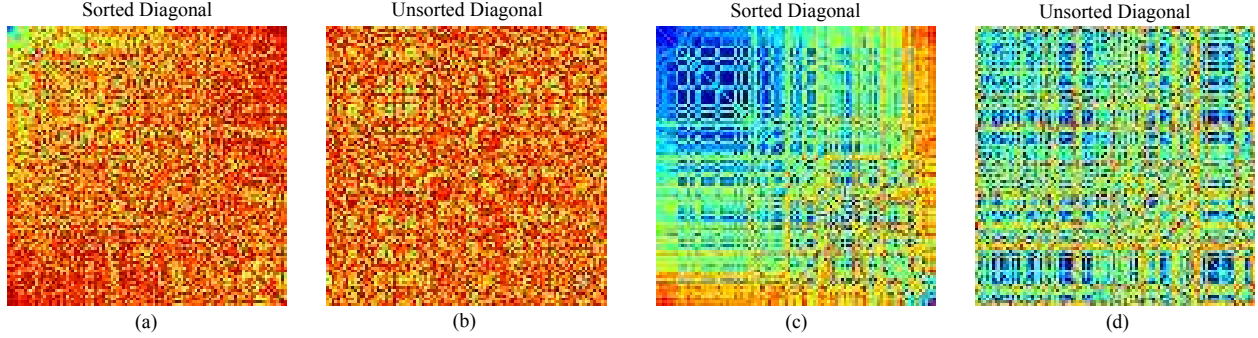


Figure 9: Effect of sorting the diagonal of Procrustes matrix on its visualization. (a) Procrustes matrix reproduced from 2(f) for the default UMAP attraction shape. The diagonal of the matrix is sorted by  $p_d$  of a sample embedding with PCA initialization. (b) The same data as in (a), but the diagonal is unsorted (or randomly sorted). (c) Procrustes matrix reproduced from 2(g) for modified attraction shape, where the diagonal of the matrix is sorted by  $p_d$  of a sample embedding with PCA initialization. (d) The same data as in (c), but the diagonal is unsorted.

$N$  embeddings obtained from random initialization. The similarity of the embeddings can be quantified by taking a mean and standard deviation of the strictly lower triangular values of the matrix  $P$  (reported as  $\text{mean} \pm \text{std}$  in Figs. 2, 10, and 11), with

$$\text{mean} = \frac{2}{N(N-1)} \sum_{i,j(i>j)} P_{i,j}, \text{ and } \text{std} = \sqrt{\sum_{i,j(i>j)} \frac{2(P_{i,j} - \text{mean})^2}{N(N-1)}} \quad (32)$$

The indexes of  $X_r$  can be sorted such that  $p_d(\{x\}_i, \{x\}_p) \leq p_d(\{x\}_{i+1}, \{x\}_p)$ , so that the diagonal values of the Procrustes matrix are given by

$$P_{i,i} = p_d(\{x\}_i, \{x\}_p) \quad (33)$$

and the off-diagonal values are given by

$$P_{i,j} = p_d(\{x\}_i, \{x\}_j). \quad (34)$$

Numerically, the sorting of the diagonal adds little value. Visually, however, the ordering reveals the underlying self-similarity of the embeddings. For example, in Fig. 9(a), the sorted diagonal shows that similar embeddings clump in the upper left region of the matrix. When we use a modified attraction shape, the number of points that are similar to each other increases (as shown by the larger blue region in Fig. 9(c)), indicating the presence of a metastable point in the embedding algorithm. On the other hand, when the diagonal is unsorted, this region disappears, and any sense of similar embeddings is lost (Fig. 9(b,d)).

## E Effect of Random Initialization in Additional Datasets

In the main text (Section 5.1), we showed results only on the MNIST dataset. Here we perform the same experiment on the Fashion-MNIST [43] and single-cell transcriptomes [44] data (Fig. 10 and 11, respectively). The main conclusion remains unchanged: modified and composite attraction shapes, such as those that increase attraction at large distances, significantly improve the consistency of reconstruction.

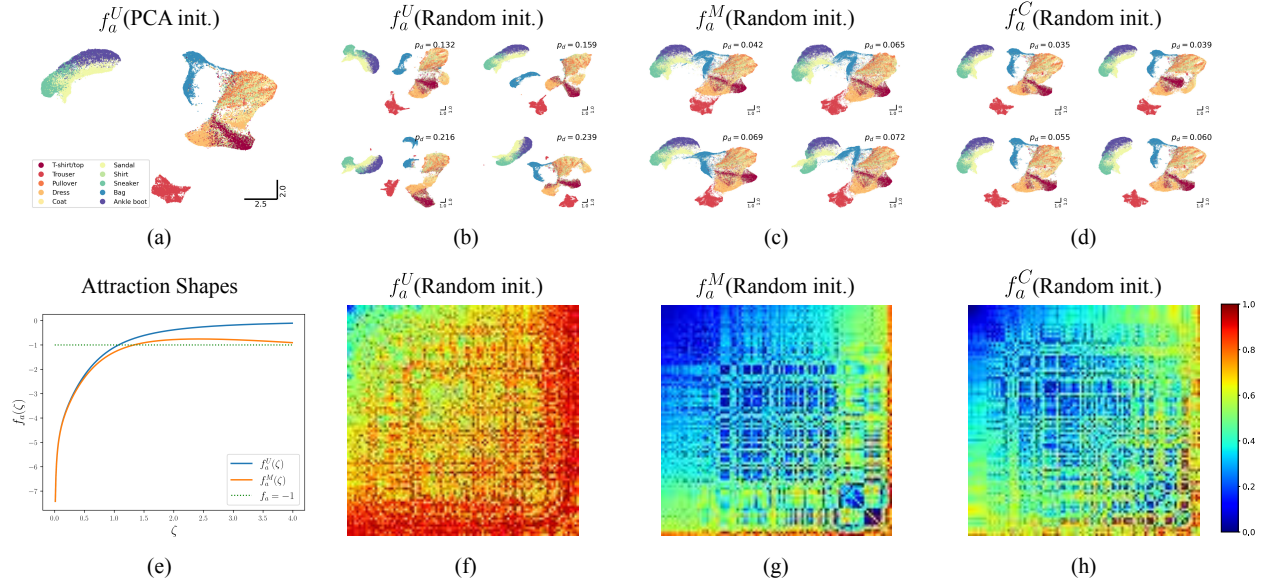


Figure 10: Effect of random UMAP initialization on different attraction shapes on FMNIST data. (a) Mapping using PCA as a standard. (b-d) Four mappings with the lowest Procrustes distance ( $p_d$ ) from the embedding in (a) for (b) default, (c) modified, and (d) composite attraction shapes. (e) Default UMAP and modified attraction shapes. (f-h) Procrustes matrix obtained from 100 runs of (f) default ( $0.72 \pm 0.15$ ), (g) modified ( $0.38 \pm 0.19$ ), and (h) composite ( $0.43 \pm 0.18$ ) attraction shapes.

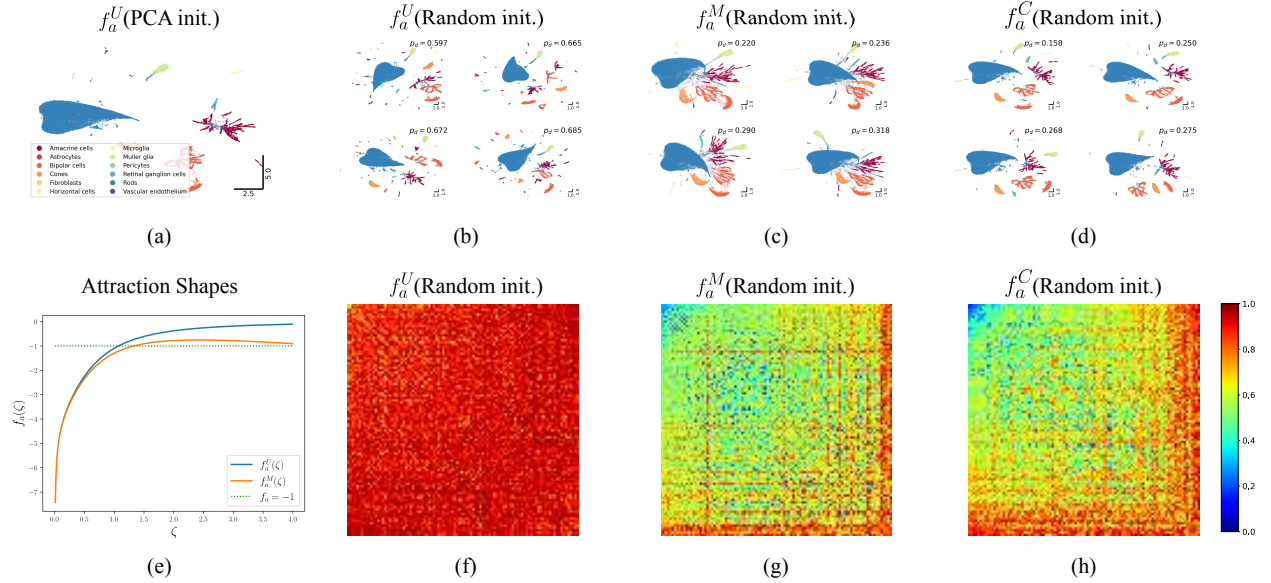


Figure 11: Effect of random UMAP initialization on different attraction shapes on single-cell transcriptomes data. (a) Mapping using PCA as a standard. (b-d) Four mappings with the lowest Procrustes distance ( $p_d$ ) from the embedding in (a) for (b) default, (c) modified, and (d) composite attraction shapes. (e) Default UMAP and modified attraction shapes. (f-h) Procrustes matrix obtained from 100 runs of (f) default ( $0.91 \pm 0.06$ ), (g) modified ( $0.61 \pm 0.13$ ), and (h) composite ( $0.64 \pm 0.15$ ) attraction shapes.

## F Alternate Dimensionality Reduction Algorithms

The alternative algorithms we consider use the same kernel function as UMAP (with  $a = 1$  and  $b = 1$  in their low-dimensional weight):

$$q_{ij} = \frac{1}{1 + \|y_i - y_j\|_2^2}. \quad (35)$$

In this section, we first discuss the TriMap [10] algorithm. Even though, this algorithm relies on triplets (and not pairwise interactions), this works as a primer for analyzing attraction and repulsion that are a bit more involved than UMAP. This discussion is followed by Pairwise Controlled Manifold Approximation (PaCMAP) [12] and its extension Pairwise Controlled Manifold Approximation with Local Adjusted Graph (LocalMAP) [15] that modify TriMAP's loss function that works for pairwise interactions. We then tackle  $t$ -SNE [45]. Finally, we provide a short note on SNE [17] that uses an alternate kernel function.

### F.1 TriMap

TriMap [10] optimizes low-dimensional using a triplet loss

$$\mathcal{L}^T = \sum_{(i,j,k)} w_{ijk} \frac{1}{1 + \frac{q_{ij}}{q_{ik}}}, \quad (36)$$

where  $w_{ijk}$  is the weight of the triplet  $(y_i, y_j, y_k)$ ,  $y_j$  is in the  $k$ -nearest neighbor set of  $y_i$  in the high dimension, and  $y_k$  is a far-away point. When minimized, we expect that  $y_i$  and  $y_j$  attract each other, while  $y_i$  and  $y_k$  repel each other. The update equations are

$$y_i^{t+1} = y_i^t + \lambda f_a^T(\zeta_1^t, \zeta_2^t)(y_i^t - y_j^t) + \lambda f_r^T(\zeta_1^t, \zeta_2^t)(y_i^t - y_k^t), \quad (37)$$

$$y_j^{t+1} = y_j^t - \lambda f_a^T(\zeta_1^t, \zeta_2^t)(y_i^t - y_j^t), \quad (38)$$

$$y_k^{t+1} = y_k^t - \lambda f_r^T(\zeta_1^t, \zeta_2^t)(y_i^t - y_k^t), \quad (39)$$

where  $\zeta_1 = \|y_i - y_j\|_2$  is the distance between nearest neighbors,  $\zeta_2 = \|y_i - y_k\|_2$  is the distance from the faraway point, and  $f_a^T$  and  $f_r^T$  are attraction and repulsion shapes of TriMap, respectively. Unlike UMAP, the attractive and repulsive components are non-separable and the shapes depend on two distance measures (making them 2D). The functional form of the attraction shape is

$$f_a^T(\zeta_1, \zeta_2) = -\frac{2(1 + \zeta_2^2)}{(2 + \zeta_1^2 + \zeta_2^2)^2}, \quad (40)$$

and the repulsion shape is

$$f_r^T(\zeta_1, \zeta_2) = \frac{2(1 + \zeta_1^2)}{(2 + \zeta_1^2 + \zeta_2^2)^2}. \quad (41)$$

The attraction and repulsion shapes (Fig. 12) of TriMap shows similar trends of that of UMAP. However, the minimum value of repulsion shape is  $-0.5$ ; thus, unlike UMAP there is no position flipping in TriMap due to attraction alone. However, since Eqs. (37-39) are not decoupled between attractive and repulsive terms, Propositions 4.1 and 4.2 do not apply. Focusing on attraction first, we show

**Proposition F.1.** *Update equations (37)-(39) provide a contraction if*

$$h_a^T(\zeta_1, \zeta_2, \theta, \lambda) < 1, \quad (42)$$

where  $h_a^T(\zeta_1, \zeta_2, \theta, \lambda) = (1 + 2\lambda f_a^T)^2 + 2(1 + 2\lambda f_a^T)\lambda f_r^T \frac{\zeta_2}{\zeta_1} \cos \theta + (\lambda f_r^T)^2 \frac{\zeta_2^2}{\zeta_1^2}$  and  $\theta$  is the angle between the vectors  $(y_i - y_j)$  and  $(y_i - y_k)$ , i.e.,  $\cos \theta = \frac{(y_i^t - y_j^t)^T (y_i^t - y_k^t)}{\|y_i^t - y_j^t\|_2 \|y_i^t - y_k^t\|_2}$ .

*Proof.* We require

$$\|y_i^{t+1} - y_j^{t+1}\|_2^2 < \|y_i^t - y_j^t\|_2^2. \quad (43)$$

From Eq. (37) and (38):  $y_i^{t+1} - y_j^{t+1} = (1 + 2\lambda f_a^T)(y_i^t - y_j^t) + \lambda f_r^T(y_i^t - y_k^t)$ . Putting this value in Eq. (43), we obtain the desired inequality.  $\square$

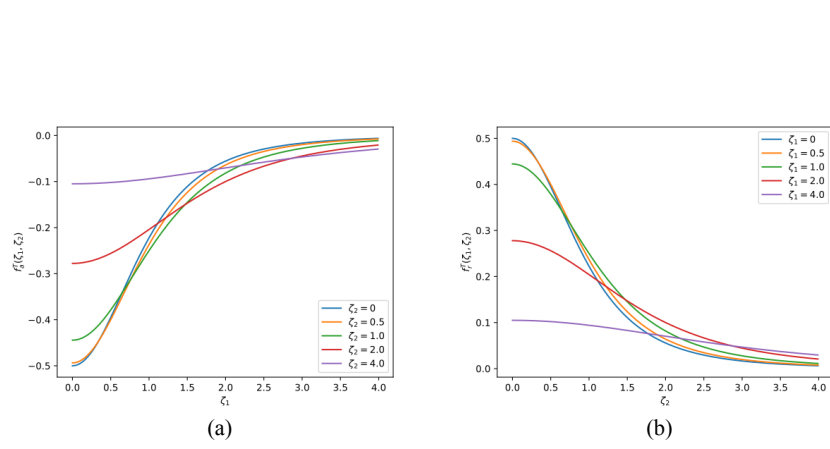


Figure 12: (a) Attraction shapes of TriMap for different  $\zeta_2$  and (b) repulsion shapes of TriMap for different  $\zeta_1$ .

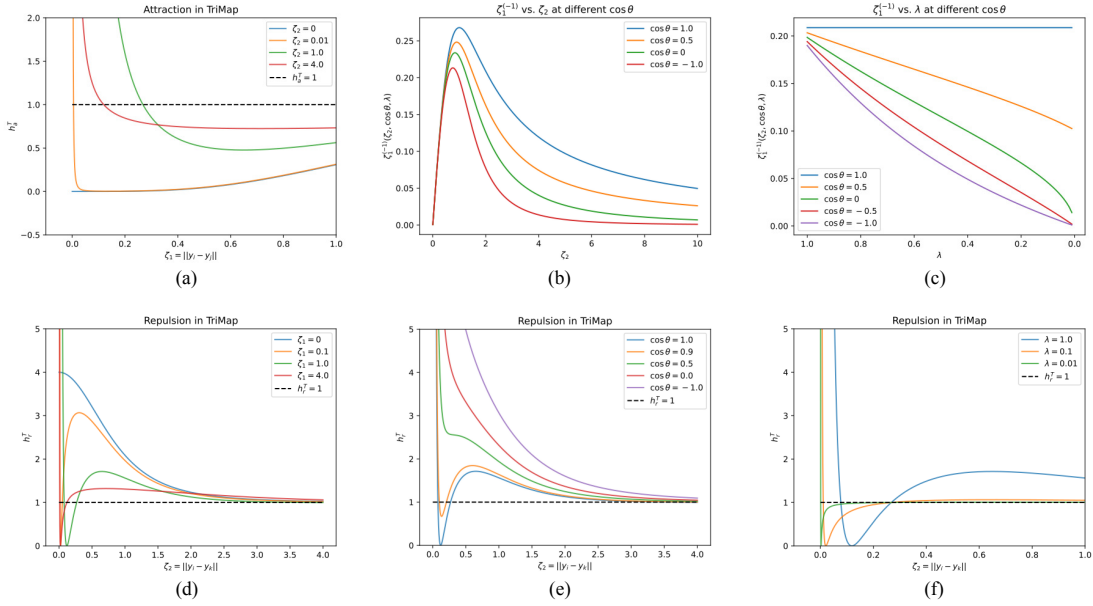


Figure 13: Attraction and repulsion behavior in TriMap. (a)  $h_a^T$  vs  $\zeta_1$  for different  $\zeta_2$ . Any values below the dotted line indicate attraction. Like UMAP, TriMap shows attraction and repulsion for nearest neighbors ( $y_i, y_j$ ). (b,c) Unlike UMAP, the minimum distance for contraction ( $\zeta_1^{(-1)}$ ) varies due to dependence on (b)  $\zeta_2$  and (c)  $\lambda$ ; the function  $\cos \theta$  regulates the range of these values. (d-f) Repulsion in TriMap by varying (d)  $\zeta_1$ , (e)  $\cos \theta$ , and (f)  $\lambda$ . Values above (below) the dotted line indicate repulsion (attraction). While the repulsion force of UMAP shows only repulsion, that of TriMap can provide both attraction and repulsion. Unless otherwise labeled,  $\zeta_1 = 1.0$ ,  $\zeta_2 = 0.5$ ,  $\cos \theta = 1.0$ , and  $\lambda = 1.0$ .



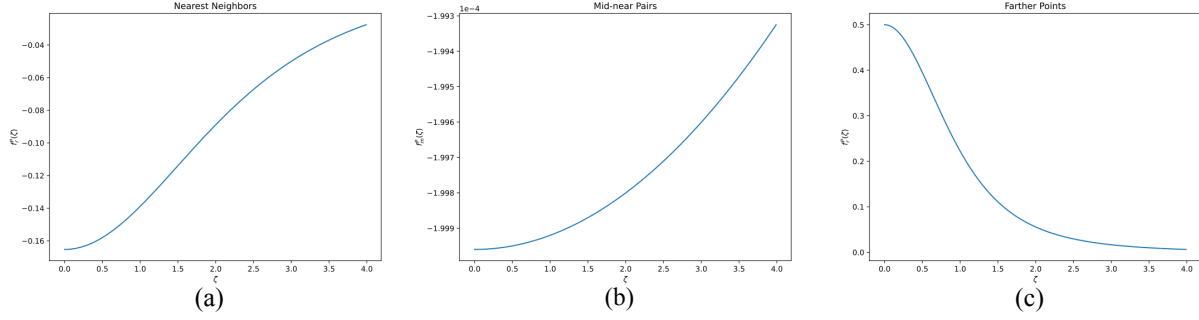


Figure 14: Attraction and repulsion shapes of PaCMAP. (a,b) Attraction shapes for (a) nearest-neighbor and (b) mid-near points (note that the values are on the order of  $10^{-4}$ ). (c) Repulsion shape for farther pairs.  $\lambda = 1$  for all figures.

Inequality (42) depends on  $\zeta_1$ ,  $\zeta_2$ ,  $\cos \theta$  and  $\lambda$ . In particular, the value of  $\zeta_1 = \|y_i - y_j\|_2$ , where we want a contraction, is coupled with additional variables. Figure 13(a) shows the attraction behavior for various values of  $\zeta_2$ , while  $\cos \theta = 1$  and  $\lambda = 1$ . The values below the dotted line indicate attraction (and thus contraction of distance  $\zeta_1$ ), whereas the values above indicate repulsion (and therefore expansion of distance  $\zeta_1$ ). The value where the dotted line and  $h_a^T$  meet gives the minimum distance for contraction ( $\zeta_1^{(-1)}$ ) [analogous to  $\zeta_{-1}$  of UMAP], which we define as

$$\zeta_1^{(-1)}(\zeta_2, \theta, \lambda) = \arg \min_{\zeta_1} |h_a^T(\zeta_1, \zeta_2, \theta, \lambda) - 1|, \quad (44)$$

$$\text{s.t. } \zeta_1 \geq 0. \quad (45)$$

$\zeta_1^{(-1)}$  has a finite value and is  $> 0$  for most cases (Fig. 13(b,c)). As a result, TriMap can show behavior similar to UMAP and thus require learning rate annealing or a similar approach (in the TriMap implementation, the authors use the delta-bar-delta [46] method under appropriate initialization).

**Proposition F.2.** *Update equations (37)-(39) provide expansion if*

$$h_r^T(\zeta_1, \zeta_2, \theta, \lambda) > 1, \quad (46)$$

where  $h_r^T(\zeta_1, \zeta_2, \theta, \lambda) = (1 + 2\lambda f_r^T)^2 + 2\lambda f_a^T(1 + \lambda f_r^T) \frac{\zeta_1}{\zeta_2} \cos \theta + (\lambda f_a^T)^2 \frac{\zeta_1^2}{\zeta_2^2}$ .

*Proof.* We require

$$\|y_i^{t+1} - y_k^{t+1}\|_2^2 > \|y_j^t - y_k^t\|_2^2. \quad (47)$$

From Eq. (37) and (39):  $y_j^{t+1} - y_k^{t+1} = (1 + 2\lambda f_r^T)(y_i^t - y_k^t) + \lambda f_a^T(y_i^t - y_j^t)$ . Putting this value in Eq. (47) we obtain inequality (46).  $\square$

Inequality (46) also depends on the set  $\zeta_1$ ,  $\zeta_2$ ,  $\cos \theta$  and  $\lambda$ . Here, we are interested in the expansion of  $\zeta_2 = \|y_i - y_k\|_2$ . Figures 13(d-f) show the repulsion behavior by varying the other quantities. Any values above the dotted line indicate repulsion (and thus expansion of distance), while the values below indicate attraction. The striking difference compared to UMAP is that repulsion in TriMap can cause contraction instead of expansion. Since this anomaly occurs for small distances, it can be avoided by an appropriate initialization and choice of triplets.

## F.2 Pairwise Controlled Manifold Approximation (PaCMAP)

PaCMAP [12] optimizes low-dimensional embedding at different scales. The loss function is

$$\mathcal{L}^P = w_{NB} \sum_{(i,j) \in NN} \frac{1}{1 + 10q_{ij}} + w_{MN} \sum_{(i,k) \in MN} \frac{1}{1 + 10000q_{ik}} + w_{FP} \sum_{(i,l) \in FP} \frac{1}{1 + \frac{1}{q_{il}}}, \quad (48)$$

where  $w_{NB}$ ,  $w_{MN}$ , and  $w_{FP}$  are weights of the nearest neighbor (NN) pairs, mid-near (MN) pairs, and further pairs (FP), respectively. The first two terms provide attraction, whereas the last term provides repulsion. A closer look at the loss function reveals that the function is a modified form of TriMap's triplet loss. For the attractive terms, it replaces TriMap's affinity for distant points with constant terms ( $1/10$  for nearest neighbors,  $1/10000$  for mid-near pairs, and  $1$



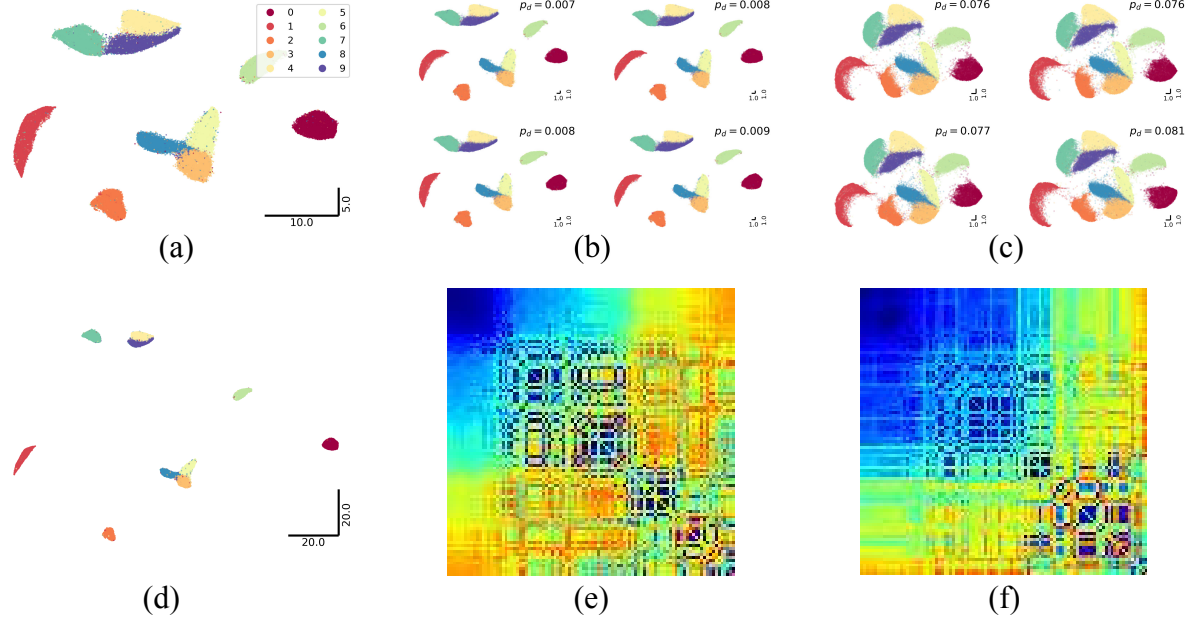


Figure 15: PaCMAP behavior for different conditions. (a) PaCMAP of MNIST data with PCA initialization. (b,c) Four samples that best match with (a) by (b) original PaCMAP and (c) PaCMAP with modified attraction shape,  $f_a^M(\zeta) = f_a^P(\zeta) - 0.001\zeta$ , when randomly initialized. (d) PaCMAP of MNIST with a modified repulsion shape  $f_r^M = f_r^P + 0.00005$ . (e,f) Procrustes matrix for (e) original PaCMAP ( $0.51 \pm 0.22$ ) and (f) PaCMAP with modified attraction shape ( $0.43 \pm 0.22$ ). Similar to UMAP, increased attraction at farther distances show improved consistency, while increased repulsion shows smaller clusters and larger inter-cluster distances.

for farther points). This loss function is thus separable into three terms and decouples the update equations. The update equations of the nearest neighbor term are

$$y_i^{t+1} = y_i^t + \lambda f_a^P(\zeta_1^t)(y_i^t - y_j^t), \quad (49)$$

$$y_j^{t+1} = y_j^t - \lambda f_a^P(\zeta_1^t)(y_i^t - y_j^t), \quad (50)$$

of the mid-near pairs are

$$y_i^{t+1} = y_i^t + \lambda f_m^P(\zeta_2^t)(y_i^t - y_k^t), \quad (51)$$

$$y_k^{t+1} = y_k^t - \lambda f_m^P(\zeta_2^t)(y_i^t - y_k^t), \quad (52)$$

and of the farthest pairs are

$$y_i^{t+1} = y_i^t + \lambda f_r^P(\zeta_3^t)(y_i^t - y_l^t), \quad (53)$$

$$y_l^{t+1} = y_l^t - \lambda f_r^P(\zeta_3^t)(y_i^t - y_l^t), \quad (54)$$

where  $\zeta_1 = \|y_i - y_j\|_2$ ,  $\zeta_2 = \|y_i - y_k\|_2$ ,  $\zeta_3 = \|y_i - y_l\|_2$  are distances,  $f_a^P$  and  $f_m^P$  are attraction shapes for nearest neighbors and mid-near pairs, respectively, and  $f_r^P$  is the repulsion shape for the farthest pairs. Correspondingly, the functional forms of the shapes are

$$f_a^P(\zeta) = -\frac{20}{(11 + \zeta^2)^2}, \quad (55)$$

$$f_m^P(\zeta) = -\frac{20000}{(10001 + \zeta^2)^2}, \quad (56)$$

$$f_r^P(\zeta) = \frac{2}{(2 + \zeta^2)^2}. \quad (57)$$

$f_a^P$  and  $f_m^P$  follow Proposition 4.1, and  $f_r$  follows Proposition 4.2 (Fig. 14). The attraction is quite low compared to UMAP, but it is good enough for a wide range of learning rates (modulated by the Adam algorithm [47]). Typically,

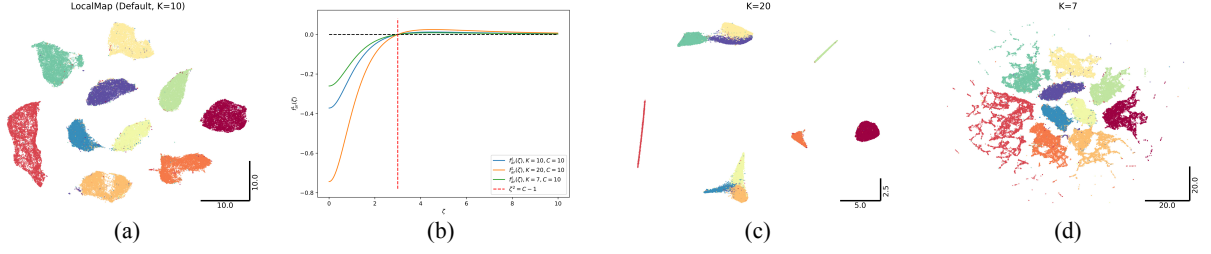


Figure 16: Behavior of LocalMAP on MNIST data. (a) Default embedding. (b) Attraction-repulsion shape of nearest neighbors. A value below (above) the dotted line indicates attraction (repulsion). Transition from attraction to repulsion occurs as  $\zeta$  increases and crosses  $\sqrt{C-1}$ . Following implementation of LocalMAP, we used  $C = 10$ . (c) When  $K$  is large ( $= 20$ ), repulsion dominates and clusters become compact. (d) When  $K$  is small ( $= 7$ ), attraction dominates and clusters break up.

PaCMAP initializes the embedding within a small sphere in the low dimension (e.g., in [12], the initialization is often on the order of  $10^{-3}$ ) and relies on repulsion to separate the individual clusters. Overall, it mostly recovers UMAP’s clustering properties (especially for MNIST). The consistency under random initialization is better than UMAP (Fig. 15(b,e)) which can be improved further using a modified attraction (Fig. 15(c,f)). Increasing repulsion by adding a small value to the repulsion shape increases compactness of the embedding (by increasing inter-cluster distance).

### F.3 Pairwise Controlled Manifold Approximation with Local Adjusted Graph (LocalMAP)

LocalMAP [15] is an iteration of the PaCMAP algorithm. One of the defining features of LocalMAP is the separation of all 10 clusters of the MNIST data (Fig. 16(a)), with behavior similar to the ones in Figs. 3(g,h,j,k) and Figs. 4(a,b). Here, we explore the interplay of attractive and repulsive forces on the compactness and connectedness of clusters.

LocalMAP performs PaCMAP and then does additional optimization on the attraction to decouple some clusters. To this end, it minimizes the following loss function

$$\mathcal{L}^L = \sum_{(i,j) \in NN} \frac{K}{\frac{1}{\sqrt{q_{ij}}} + C\sqrt{q_{ij}}} + \sum_{(i,l) \in FP} \frac{1}{1 + \frac{1}{q_{il}}}. \quad (58)$$

The first term amalgamates the attractive and repulsive nature of the triplet loss function that works on the same pair. In one regime, this function causes attraction, while in the other, it causes repulsion. The second term is identical to the ones in PaCMAP; the only difference is that the algorithm resamples further pairs every few iterations. Thus, we analyze only the first term involving nearest neighbors. The update equations are

$$y_i^{t+1} = y_i^t + \lambda f_{ar}^L(\zeta_1^t)(y_i^t - y_j^t), \quad (59)$$

$$y_j^{t+1} = y_j^t - \lambda f_{ar}^L(\zeta_1^t)(y_i^t - y_j^t), \quad (60)$$

where  $f_{ar}^L$  is the attraction-repulsion shape given by

$$f_{ar}^L(\zeta) = -\frac{K(C-1-\zeta^2)}{2\sqrt{1+\zeta^2}(1+C+\zeta^2)^2}. \quad (61)$$

The update provides contraction as long as  $\zeta^2 < C-1$  and  $-1 < \lambda f_{ar}^L < 0$  (from Proposition 4.1). When  $\zeta^2 > C-1$ ,  $f_{ar} > 0$ , and by Proposition 4.2 the update equations provide expansion. The values of  $K$  and  $C$  determine whether attraction or repulsion dominates the dynamics. In LocalMAP implementation, both  $C$  and  $K$  are set to 10 (Fig. 16(b)), and the strength of attraction is higher than PaCMAP (Fig. 14(a)). As a result, when  $\zeta > 3$ , the nearest neighbors face repulsion, causing pairs bridging two clusters to separate. The value of  $K$ , working as a scaling parameter for the forces, regulates this separation.

Using Proposition 4.1,  $\lambda f_{ar}^L(0) \geq -\frac{1}{2}$  gives the maximum values of  $K$ , and the maximum attraction possible by  $f_{ar}^L$ , without flipping the placements of the pairs. (We would want to avoid flipping the pairs at the LocalMAP optimization to preserve the ordering from PaCMAP; otherwise, it may inhibit cluster separation.) This simplifies (61) to  $K \leq \frac{\lambda(1+C)^2}{C-1}$ , which for  $C = 10$  and  $\lambda = 1$  gives  $K \lesssim 13.44$ . Moreover, at a higher value of  $K \gtrsim 13.44$ , the repulsive forces

dominate, and the clusters become more compact, but objective of LocalMAP fails (the bridge between clusters persists in Fig. 16(c) for  $K = 20$ ). On the other hand, as  $K$  decreases, attractive forces dominate (because repulsive forces are too low), and the embedding shows the breaking up of existing clusters (Fig. 16(d) for  $K = 7$ , which mimics the one in Fig. 4(b)).

#### F.4 $t$ -distributed Stochastic Neighbor Embedding ( $t$ -SNE)

$t$ -SNE [45] optimizes pairwise distances. The loss function is

$$\mathcal{L} = - \sum_{i,j} w_{i,j} \log \left( \frac{q_{i,j}}{\sum_{k \neq l} q_{k,l}} \right), \quad (62)$$

where  $w_{i,j}$  is the weight of the pair. The original implementation of  $t$ -SNE considers all the pairs (not just nearest neighbors). This loss function decomposes into attraction and repulsion forces by

$$\mathcal{L} = \sum_{i,j} \left[ -w_{i,j} \log(q_{i,j}) + w_{i,j} \log \left( \sum_{k \neq l} q_{k,l} \right) \right]. \quad (63)$$

As previously, the first term provides the attractive forces and the second term provides the repulsive forces. While the attractive term is identical to that of UMAP (with  $a = 1$  and  $b = 1$ ) and is easy to compute, the repulsive term is coupled among every pair and thus, is very costly. Using the same principles we applied for UMAP, we can write the update equations of  $t$ -SNE. Since the original  $t$ -SNE didn't rely on the nearest neighbor graph, the weight  $w_{i,j}$ , computed for all the pairs, is important in the update equations. The attractive update equations are

$$y_i^{t+1} = y_i^t + \lambda w_{i,j} f_a^{t-SNE}(\zeta_{i,j}^t)(y_i^t - y_j^t), \quad (64)$$

$$y_j^{t+1} = y_j^t - \lambda w_{i,j} f_a^{t-SNE}(\zeta_{i,j}^t)(y_i^t - y_j^t), \quad (65)$$

where  $f_a^{t-SNE}$  is the attraction shape of  $t$ -SNE and  $\zeta_{i,j} = \|y_i - y_j\|_2$ . The update equation for the repulsive parts are

$$y_i^{t+1} = y_i^t + \lambda \frac{w_{i,j}}{Z} \sum_k f_r^{t-SNE}(\zeta_{i,k}^t)(y_i^t - y_k^t), \quad (66)$$

$$y_j^{t+1} = y_j^t - \lambda \frac{w_{i,j}}{Z} \sum_l f_r^{t-SNE}(\zeta_{l,j}^t)(y_l^t - y_j^t), \forall j, j \neq i, \quad (67)$$

where  $f_r^{t-SNE}$  is the repulsion shape of  $t$ -SNE and  $Z = \sum_{k \neq l} q_{k,l}$ . The functional forms of these shapes are

$$f_a^{t-SNE}(\zeta) = -\frac{2}{1 + \zeta^2}, \text{ and} \quad (68)$$

$$f_r^{t-SNE}(\zeta) = \frac{2}{(1 + \zeta^2)^2}. \quad (69)$$

From the attractive update Eqs. (64)-(65),  $f_a^{t-SNE}$  follows Proposition 4.1 (with  $0 < \lambda w_{i,j} f_a^{t-SNE} < -1$ ) and gives the minimum distance for contraction,  $\zeta_{-1}$ ). The repulsive update is coupled with all the pairs and thus does not have a simple relation to the repulsion shape. Rather, enabled by our experience from TriMap's analysis, we can derive the following:

**Proposition F.3.** *The update Eqs. (66)-(67) provide an expansion if*

$$h_r^{t-SNE}(\zeta_{i,j}, v, \theta, \lambda, w_{i,j}) > 1, \quad (70)$$

where,  $h_r^{t-SNE}(\zeta_{i,j}, v, \theta, \lambda, w_{i,j}) = (1 + 2\lambda \frac{w_{i,j}}{Z} f_r^{t-SNE}(\zeta_{i,j}))^2 + \frac{\|v\|_2^2}{\zeta_{i,j}^2} + 2\lambda \frac{w_{i,j}}{Z} f_r^{t-SNE}(\zeta_{i,j}) \frac{\|v\|_2}{\zeta_{i,j}} \cos \theta$ ,  $v = \lambda \frac{w_{i,j}}{Z} \left( \sum_{k, k \neq j} f_r^{t-SNE}(\zeta_{i,k})(y_i - y_k) + \sum_{l, l \neq i} f_r^{t-SNE}(\zeta_{l,j})(y_l - y_j) \right)$ , and  $\theta$  is the angle between  $(y_i - y_j)$  and  $v$ .

*Proof.* We require,

$$\|y_i^{t+1} - y_j^{t+1}\|_2^2 > \|y_i^t - y_j^t\|_2^2 \quad (71)$$

From Eqs. (66) and (67),  $y_i - y_j = (1 + 2\lambda \frac{w_{i,j}}{Z} f_r^{t-SNE}(\zeta_{i,j}))(y_i - y_j) + v$ . Putting this value in Eq. (71), we obtain the desired inequality.  $\square$

Since  $t$ -SNE’s condition for repulsion (Eq. 70) resembles that of TriMap, the repulsion behavior will be the same. Thus,  $t$ -SNE’s repulsive forces can give both attraction and repulsion.

Since,  $t$ -SNE’s forces are scaled (by  $w_{i,j}$  for attraction and  $\frac{w_{i,j}}{Z}$  for repulsion), the attractive and repulsive forces are typically lower than that of UMAP. As a result, the algorithm generally uses large values for learning rate (e.g.,  $\approx 10^3$  in the Open- $t$ -SNE package [48]). Moreover, most  $t$ -SNE implementations require an ‘early exaggeration’ step where the attractive forces are multiplied by a constant value for the first few iterations. This causes points that are supposed to be closer but currently placed far apart to approach each other (inducing far-sightedness). On the other hand, if some points are very close ( $\zeta_{i,j} \approx \zeta_{-1}$ ) but require separation, this early exaggeration trick achieves that as well. Thus, ‘early exaggeration’ plays a vital role in finding a consistent embedding in  $t$ -SNE and is an indispensable feature of the algorithm; especially when initialized randomly. (This trick, when applied throughout the optimization, makes  $t$ -SNE embeddings look closer to UMAP embeddings [26].)

## F.5 Stochastic Neighbor Embedding (SNE)

SNE [17] is one of the oldest algorithms in this class. This follows the same formula of  $t$ -SNE (Eq. 63), but with  $q_{i,j} = \exp(-||y_i - y_j||_2^2)$ . This results in the attraction shape

$$f_a^{SNE}(\zeta) = -2, \quad (72)$$

that follows Proposition 4.1 (with  $0 < \lambda w_{i,j} f_a^{SNE} < -1$ ) and the repulsion shape

$$f_r^{SNE}(\zeta) = 2 \exp(-\zeta^2), \quad (73)$$

that follows proposition F.3 (by replacing the  $t$ -SNE symbols with SNE counterparts). The attraction shape is ill-posed and thus mainly relies on the values of learning rate ( $\lambda$ ) and the weights ( $w_{i,j}$ ) for contraction resulting in clusters overlapping each other even for small number of samples (called crowding problem [45]), which  $t$ -SNE and the subsequent algorithms improve by moving away from the Gaussian kernel and using Eq. (35).

## G Implementation Details

For analysis, we implemented our own UMAP algorithm. We used numba [49] to compute an exact nearest neighbor graph (instead of an approximate one) with  $k = 15$  and scikit-learn’s implementation of the PCA algorithm [50] for PCA initialization. We used this to produce and quantify the embeddings in Figs. 2, 3, 4, 7, 10, 11, and 9.

The mappings shown in Figs. 2, 3, 10, 11, and 15 are rotated to a reference embedding ((a) for each respective Figures). To achieve this, we performed Procrustes alignment of the embeddings by normalizing them (zero mean and unit norm) and then using SciPy’s [51] `orthogonal_procrustes` method to extract rotation and scaling parameters.

To compare with Neg- $t$ -SNE in Fig. 5, we used the author’s implementation of the contrastive embedding framework for both the UMAP and the Neg- $t$ -SNE algorithms (available at <https://github.com/berenslab/contrastive-ne>).

PaCMAP and LocalMAP embeddings in Figs. 15 and 16 were obtained using the official PaCMAP package (available at <https://github.com/YingfanWang/PaCMAP>).

The codes for displaying the embeddings of the PubMed dataset in Fig. 8 are adapted from <https://github.com/berenslab/pubmed-landscape>.